CHAPTER 5
PRACTICAL APPLICATION OF DISCONTINUUM MODELLING

5.1 MODELLING OF SAND SAMPLE

5.1.1 INTRODUCTION

High quality of the sampling, which requires that the sand sample is undisturbed, seems considerably difficult. But, it is quite significant in evaluating the strength characteristics of sand such as the liquefaction resistance. Although many studies on sand sampling have been made so far (e.g. Zen et al., 1981 among others), there are still lots of subjects unsolved

In this study, we mainly investigate the characteristics of sand sampling disturbance with the relationships of the samplers and the sampling ways so that we can provide useful information for developing a new sand sampling technology. At first, laboratory experiments using two dimensional model ground composed of aluminum bars are carried out. And then, the experiments are simulated by using the distinct element method (DEM) (Cundall,P.A, 1971, 1979). By comparing the results obtained by numerical simulation with those from the experiments, we found that they are in good agreement. Thus, DEM can be used for investigating the sand sampling disturbance. Since the movement of individual sand particle can be shown very clearly and it is easy to make models for various cases, finally, DEM simulations are carried out for many cases. The influential factors on sample disturbance such as the dimension of sampler, penetration velocity, particle size and the relative density are analytically examined in this paper.

5.1.2 MODEL EXPERIMENT AND ANALYSIS
Equipment and Test Procedure
The experimental equipment is shown in Photo 5.1.1. and the schematic diagram of experimental setup is shown in Fig.5.1.1. The two dimensional model ground is composed of aluminum bars, which are 50mm long with two kinds of diameters: 1.0mm and 2.0mm. The grained bars are so gently piled up that the model layer is of the initial relative density of 75%. The dimension of model ground is 600mm wide, 400mm high and 50mm thick. In the experiments, four types of model samplers shown in Fig.5.1.1 are used. The sampler is penetrated up to 20cm deep from the ground surface with a constant velocity in each case of experiments. During the penetration, the displacements of aluminum bars are recorded with a digital vide camera. The penetration resistance and the displacement of sampler are measured by using a load cell and several displacement gauges, respectively. One of examples for deformation during sampling in experiment is shown by Photo 5.1.2.Five cases of experiments have been carried out and they are simulated by using DEM (Table 5.1.1).
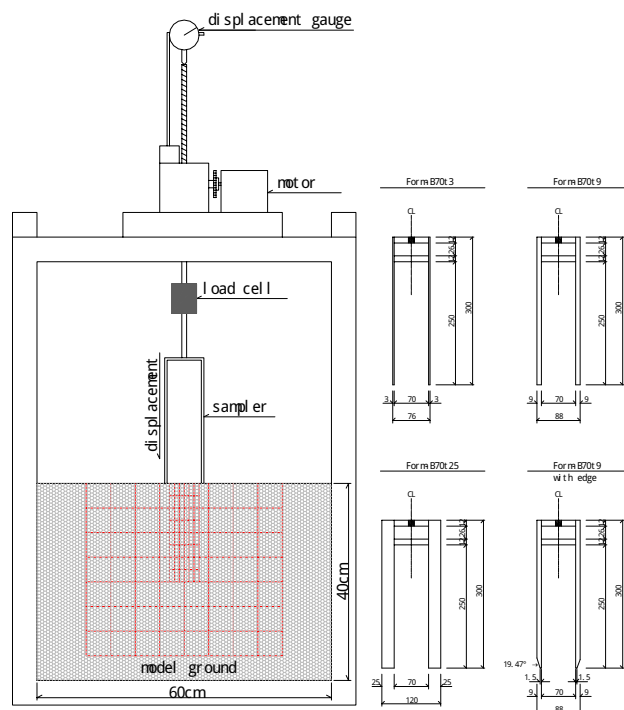

Photo 5.1.1 The experimental equipment.

Fig.5.1.1 Schematic diagrams of equipment and model sand samplers used

Table 5.1.1 The cases of Experiments & analysis

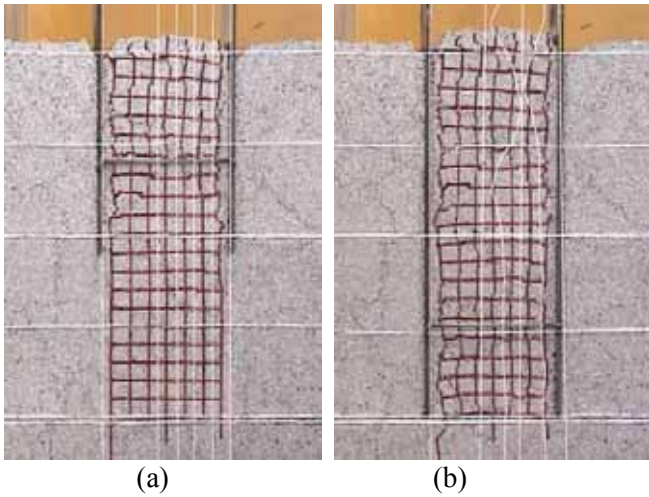| Experimental No.	Thickness of sampler	Penetration speed	Relative density	Particle size
Experiment1	3mm			
Experiment2	9mm			
Experiment3	25mm	3mm/min (0.05cm/s)		2mm
Experiment4	9mm-edge			
Experiment5	3mm			1mm
DEM1	3mm		75%	
DEM2	9mm			
DEM3	25mm	5cm/s		2mm
DEM4	9mm-edge			
DEM5	3mm			1mm

Photo 5.1.2. Deformations of the model ground with penetrations of 10cm (a) and 20cm (b) during sampling.

Numerical Analysis

The two dimensional distinct element method (DEM) is applied to simulate the experiments. The model ground, the 400mm width and the 400mm height, was generated by free falling of particles. The parameters used for the analysis are shown in Table 2, where k_n is the normal stiffness and k_s is the shear stiffness of the contact springs, ϕ_μ is the friction angle, ρ is the density of particles.

Table 5.1.2 Parameters used for the DEM analysis

Constant	Using value
k_n, k_s	$1.0 \times 10^8 (N/m)$
ϕ_μ	$16°$
ρ	$2.690 (g/cm^3)$

Comparison between Experiment and Numeric Results
Both the results from both the experiment and the corresponding numerical analysis are shown in Figs.5.1.2 and 3. In this case, the sampler with 70mm of inner diameter and 3mm of thickness is used to penetrate into the model ground, which is composed of 70 thousands of aluminum bars with 2mm diameter.
The vectors represent the displacements and the contour maps represent strains for both the experiment and the numerical analysis in Fig.5.1.2. It can be seen that the displacement vectors are of the same pattern. Therefore, the displacements from experiment and numeric analysis are in good agreement each other.
In addition, the distributions of shear strain in Fig.5.1.2 show that there are the disturbed areas along the inside wall of the sampler. The area with high density is located at the depth of around -15cm, which could be attributed to the clogging of the sampler during the sampling penetration.
Fig.5.1.3 shows the displacements of the particles (bars) along the deep direction after the 20cm
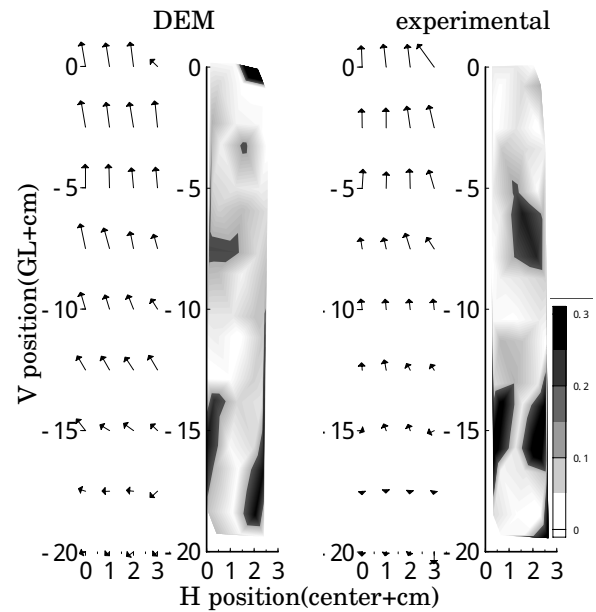

Fig.5.1.2 The displacements and strains from both the experiment and the corresponding DEM analysis.
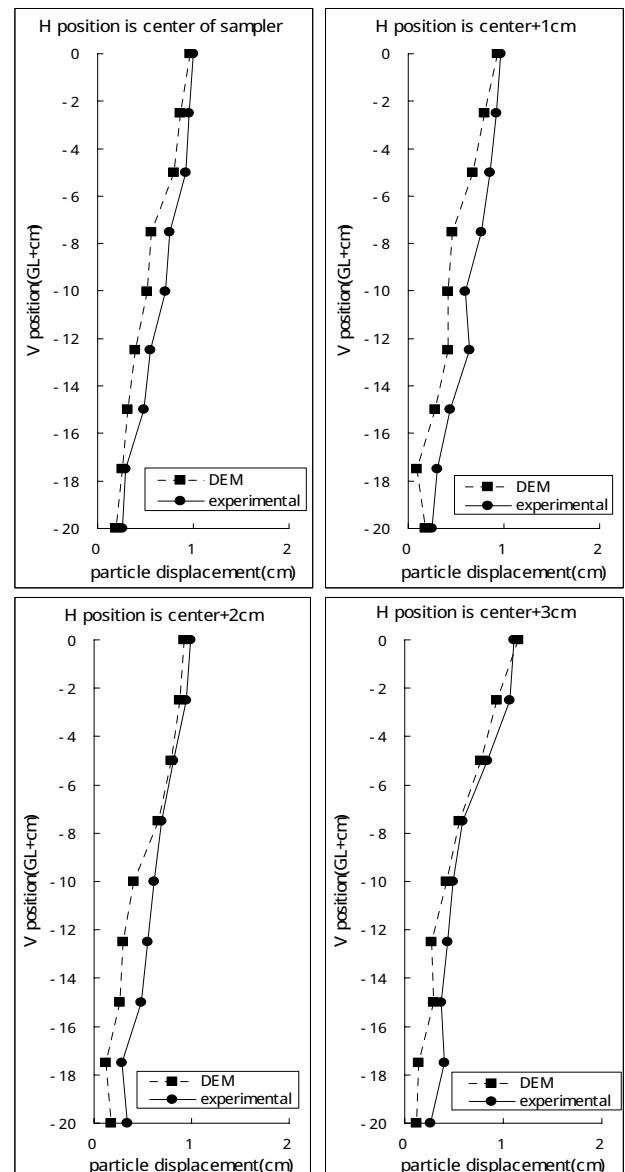

Fig. 5.1.3 Displacements along the vertical directions for different locations.

penetration for the locations: the center of the sampler, 1cm, 2cm and 3cm apart from the center, respectively. The displacements obtained from both the experimental and the DEM are in good agreement each other. Since the same results have also been obtained for the other cases, it has been shown that DEM is one of the effective numerical analysis methods for simulating the movements of particles.

5.1.3 NUMERICAL EVALUATION

.

As the effectiveness of DEM has been confirmed in the former chapter, the more detailed analysis is carried out under various conditions. In these DEM simulations, the prospected major influential factors such as the relative density, particle size, diameter of sampler and penetration velocity are evaluated. Ten cases of DEM calculations shown in Table 5.1.3 have been carried out.

Table 5.1.3 The cases of DEM numerical simulations

No.	Thickness of sampler	Penetration velocity	Relative density	Particle Size
D1	3mm	5cm/s	75%	2mm
D2	9mm			
D3	25mm			
D4	3mm	10cm/s		
D5		20cm/s		
D6		5cm/s	25%	1mm
D7				2mm
D8				3.2mm
D9			75%	1mm
D10				3.2mm

The parameters used for the analysis are listed in Table 5.1.4, where ϕ_μ is the sand particle friction angle.

Table5.1. 4 Parameters for DEM simulations

constant	Using value
k_n, k_s	$1.0 \times 10^8 (N/m)$
ϕ_μ	$30°$
ρ	$2.600 (g/cm^3)$

The variation of void ratio was calculated with the specimen taken from the edge of sampler, as an index to evaluate the sample disturbance. The size of specimen along the center axis of the sampler was 100mm high and 50mm wide.

Effect of Thickness of Sampler
Fig.5.1.4 shows the relationship between the void ratio and wall thickness of sampler. The variation of void ratio is expressed by the non-dimensional parameter, $e_{p\max}/e_0$ or $e_{p\min}/e_0$ normalized with the initial void ratio e_0. The $e_{p\max}$ and $e_{p\min}$ are respectively the maximum and minimum void ratios during sampler penetration. The normalized void ratio means the

compression of sample when it reveals smaller than 1.0 and the expansion when it is greater than 1.0. The horizontal axis is represented by the non-dimensional radius of sampler, r_{in}/r_{out}, where r_{in} and r_{out} denote respectively the inner and outer radius of sampler. In Fig.4, it is found that the variation of void ratio increases linearly with increasing thickness of sand sampler, say, decreasing value of the r_{in}/r_{out}. This suggests that the small wall thickness of sampler, such as the thin wall sampler, is better than the thicker wall sampler for obtaining a high quality of undisturbed sample.
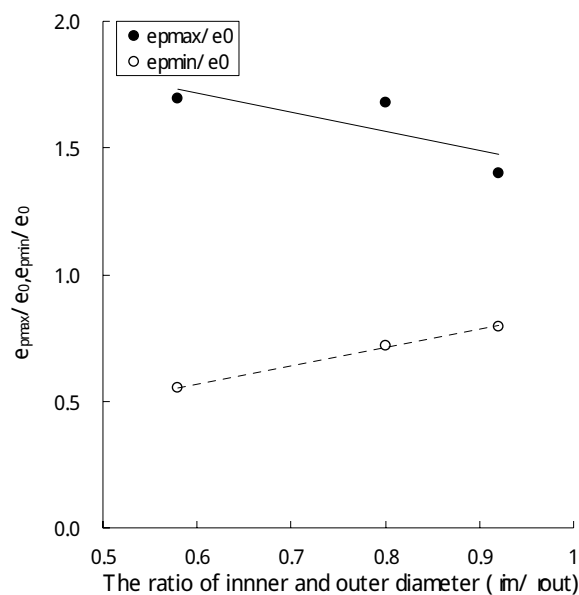

Fig.5.1.4 Effect of wall thickness of sampler

Effect of Penetration Velocity
Fig.5.1.5 shows the effect of penetration velocity of sampler on the normalized void ratio.
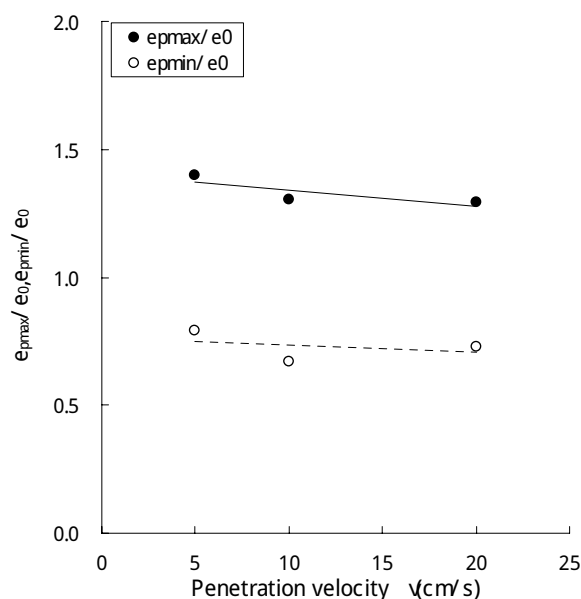In this analysis, the clear effect can not be recognized

Fig.5.1.5 Effect of penetration velocity

in the relationship between the normalized void ratio and penetration velocity. The effect of penetration velocity on the change of void ratio may be considered

to be extremely small.

Effect of Particle Size
The effect of particle size on the normalized void ratio is presented in Fig.6. The width of sampler used in the analysis was 70mm. Uniform model ground composed of a single particle size of respectively 1mm, 2mm and 3.2mm was analyzed. Fig.6 indicates that the normalized void ratio ($e_{p\max}/e_0$) increases linearly with increasing particle size. Namely, in the case of large particle size, the change of void due to the penetration of sampler becomes larger. According to the analysis, the reason of this trend is considered like this; when the particle size becomes larger, the contact stresses during the penetration of sampler become larger as well. As the result, it causes a large strain of sample.

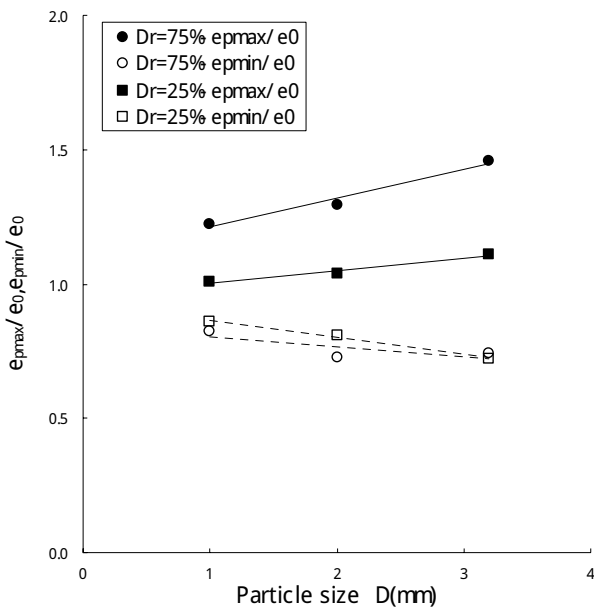Fig.5.1.7 Effect of relative density

Fig.5.1.6 Effect of particle size

Effect of Relative Density
Fig.5.1.7 shows the effect of the relative density on the normalized void ratio. When the relative density increases, the normalized void ratio indicates greater values, especially in the expansion side. On the other hand, in the compressive side, the effect seems to be almost the same, irrespective of the relative density.

An example of sampler selection
From the analytical results presented in Figs.5.1.4 to 7, the relationships between the non-dimensional size (particle size/inner diameter of sampler), the relative density and the void ratio change were drawn in Fig.5.1.8.
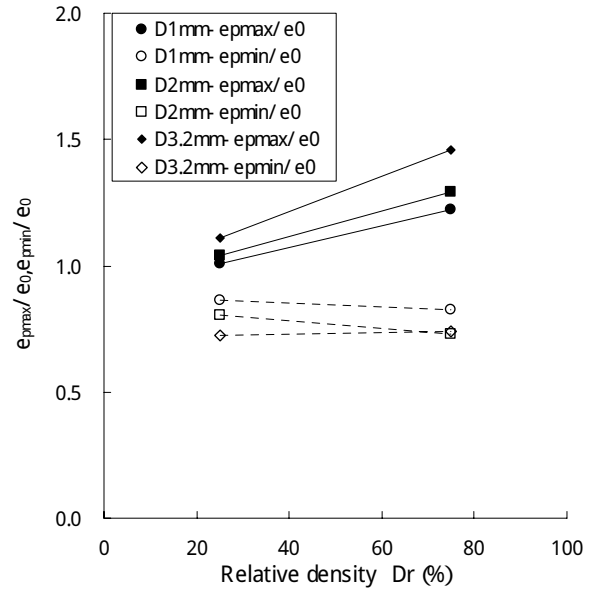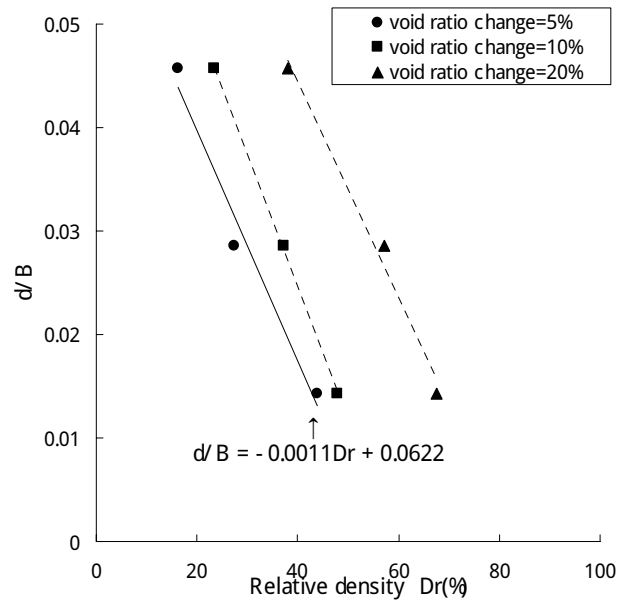

Fig.5.1.8 Relationships between the particle size/inner diameter of sampler, relative density and void ratio change.

It could be said that the size of sampler has to be selected, depending on the particle size and the relative density of ground. Namely, if the change of void ratio is required to restrain less than 5%, the following condition is to be satisfied; d/B ≦ -0.0011Dr + 0.0622. Therefore, the inner diameter of sampler, B ≧ d/(-0.0011Dr + 0.0622) is obtained. Where, d is the particle size, B is the inner diameter of sampler.
It should be noted that the equation is derived for a realistic model ground composed of uniform single particle size. Further study is needed for practical application.

5.1.4 CONCLUSION

In this study, the disturbance of sand sampling has been investigated by both the experiments and DEM numerical analysis. By comparison between the results from the experiments and DEM simulations, we confirmed that DEM is applicable to this kind of problems. Therefore, the detailed analysis has been made by only DEM. The effects of major influential factors have been quantitatively evaluated. As an index, the normalized void ratio was adopted to evaluate the sample disturbance. The major conclusions obtained from the study are as follows:

i) The variation of void ratio increases linearly as the wall thickness of sand sampler increases,

ii) The effect of penetration velocity of sampler on the variation of void ratio is found not very much.

iii) The relative density causes large variation of void ratio, especially in the expansion side. On the other hand, in the compressive side, the variation rate seems to be almost the same, irrespective of the relative density.

An example of sampler selection procedure has been demonstrated. The effectiveness of this approach has been shown.

REFERENCE

Cundall,P.A (1971). A computer model for simulating progressive, large scale movement in blocky rock system, *Symp. ISRM, Vol.2, pp129 ~ 136.*

Cundall, P. A., and Strack, O. D. L. (1979). A discrete numerical model for granular assemblies', Géotechnique 29, No. 1, 47-65.

Zen, K. ets.al. (1981). Attempts on sand sampling and quality evaluation, Proc. of Sand Sampling Symposium, Japanese Geotechnical Society, pp.55 ~ 62. (in Japanese)

Yamamoto S. and Matsuoka H. (1995). A numerical bearing capacity test by dem on granular assembles with sandbag-like reinforcement, *Journal of Geotechnical Engineering , No.529/Ⅲ-33,125-134. (in Japanese)*

Note: There is a co-author of this paper as follows

K. Hiramatsu Wesco, Co., Okayama, Japan

5.2 A NUMERICAL STUDY ON THE DEM PARAMETERS FOR A RUBBLE MOUND

5.2.1 INTRODUCTION

A rubble mound which is composed of a small rock assembly is a fundamental structure supporting a large gravity structure such a caisson. In the past, several researches have been done to clarify the bearing capacity and behaviour of rubble mounds. Recently, it has come to be able to simulate the behaviour of rubble grains by DEM (Distinct Element Method). DEM is suitable for the simulation of granular materials like rubble grains. In this method, it is easy to consider the deformability and changeability of supporting formation in the rubble mound due to the weight of the structure and the external forces of waves. In the DEM method, not only circular or sphere particles but also ellipse elements and arbitrarily shaped elements which are composed of some number of particles are used in these days. Furthermore, in order to represent break-up grains, there are some researches which deal with bonded particles. Bonds can be envisioned as a kind of glue joining the two particles. Damage is represented explicitly as broken bonds. The practical behaviour of such models is affected by the grain size, shape and packing conditions. It is also unclear how to specify the DEM parameter such as normal stiffness, tangential stiffness and particle friction coefficient.

In general, the bulk properties of any given synthetic material can be determined by performing a series of biaxial tests on that particular material. These tests are performed numerically and designed to simulate similar tests performed in the laboratory.

In this research, in order to investigate and clarify the relationship between the DEM parameters and the bulk properties such as elastic modulus and poison's ratio, a series of the biaxial tests were performed using the rubble grains.

5.2.2 BIAXIAL TEST SIMULATION

Biaxial test simulations were carried out to investigate the influence of the DEM parameters. In this simulation, a specimen of synthetic material is represented as an assembly of circular particles. Each particle is modelled as a disk of unit thickness with linear contact springs. In this paper, grain crushability does not take part into account. In the future, it is necessary to consider particle crushability with bonded breakage model. The bonded model should be used linear contact model which are governed through the linear contact law of the particles. Therefore, the focused DEM parameters are normal and shear stiffness (kn and ks) and surface friction coefficient (μ).

The specimen is confined and loaded by pair of opposing frictionless walls. Figure 5.2.1 shows the grain size distribution (Kobayashi 1987). Using this distribution, the number of the particles in the sample is 2517 as shown Figure 5.2.2..

Table 5.2.1 shows a one of actual rubble properties. The elastic properties and strength which are calculated by the DEM results were compared with these properties.

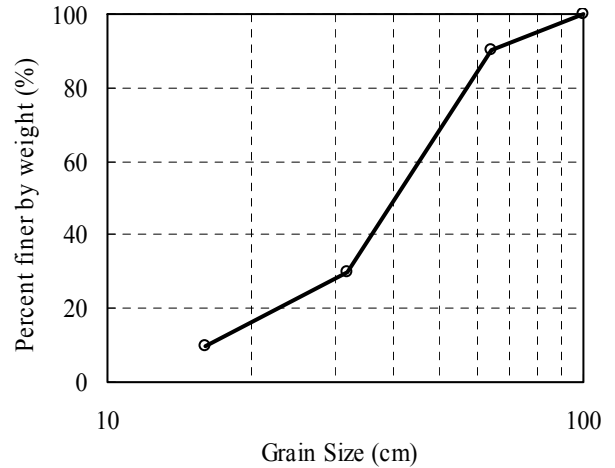Table 5.2.2 shows DEM parameters for parametric study of the biaxial simulations.

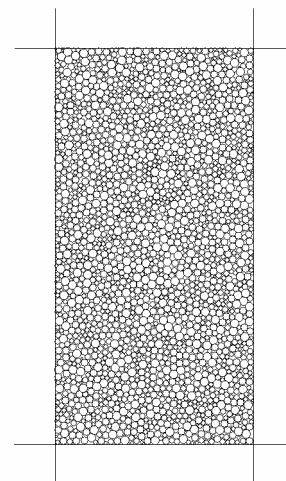Figure5.2. 1 Grain size distribution curves

Figure 5.2.2 Particle assembly

Table 5.2.1. Rubble properties

Young's modulus(E)	1e5	(kPa)
Poisson's ratio(ν)	0.35	
Apparent cohesion	20.0	(kPa)
Internal friction angle (ϕ)	35	(degrees)

Table 5.2.2. Biaxial test cases

Normal stiffness(kn)	1e7,1e8,1e9	(N/m)
Ratio of shear stiffness(ks/kn)	1/10,1/5,1/4,1/2,1/1	
Particle friction coefficient	0.5,1.0,1.5,3.0	
Confining pressure ($\sigma3$)	100,200,300,500	(kPa)

5.2.3 NUMERICAL RESULTS

A series of tests were performed to compare the elastic properties and failure strength with the macro rubble properties. The elastic properties of the numerical sample can be determined by performing load/unload test under elastic condition. The elastic condition is controlled given to the high bond strength and no sliding at all contacts between particles. Young's modulus(E) and Poisson's ratio(ν) of the sample are obtained from following equations.

$$E = \frac{\Delta\sigma_a}{\Delta\varepsilon_a} \qquad (5.2.1)$$

$$\nu = 1 - \frac{\Delta\varepsilon_v}{\Delta\varepsilon_a} \qquad (5.2.2)$$

σ_a is axial deviatoric stress, ε_a is axial strain and ε_v is volumetric strain.

Elastic properties

Figure 5.2.3 shows the relationship between the ratio ks/kn and Young's modulus which is calculated from biaxial simulation results using Eq.(5.2.1) when the confining pressure is 100kPa. The calculated Young's modulus is affected by the normal stiffness kn. It seems to appear the linear relationship between Young's modulus and particle normal stiffness. The shear stiffness ks does not have a much effect on Young's modulus.

Figure 5.2.4 shows the relationship between the ratio ks/kn and Poisson's ratio. The Poisson's ratio is strongly affected by the fraction of normal and shear stiffness. As the fraction ks/kn increase, evaluated poison's ratio decreases.

According to table 1, Young's modulus and Poisson's ratio of the actual rubble property are 1e8(Pa) and 0.35 respectively. Therefore, the normal stiffness can be specify the value between 1e8(N/m) and 1e9(N/m). The ratio ks/kn can be chosen the value between 0.25 and 0.4.

Next, in order to examine the effect of confining pressure, correlation between the elastic property and the ratio ks/kn at each confining pressure are shown as figure 5.2.5 and figure5.2. 6.

Figure 5.2.5 shows the correlation between Young's modulus and the ratio ks/kn when the normal stiffness of particles is 1e8(N/m). Figure 5.2.6 shows the correlation about Poisson's ratio. As confining pressure increases, calculated Young's modulus of particles also increase. The effect of the confining pressure on normal stiffness is small. Besides, the confined stress increase, the evaluated poison's ratio decreases
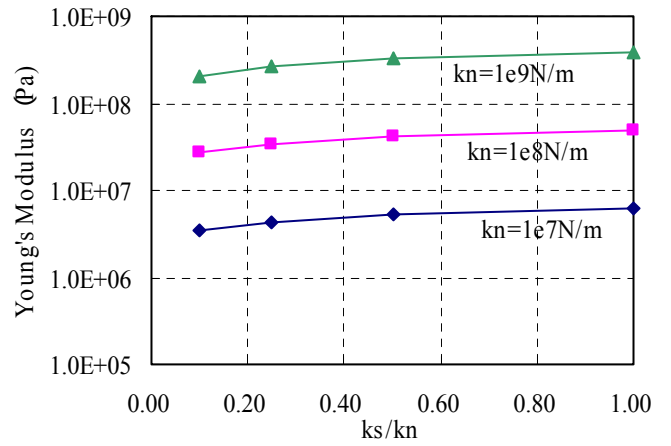

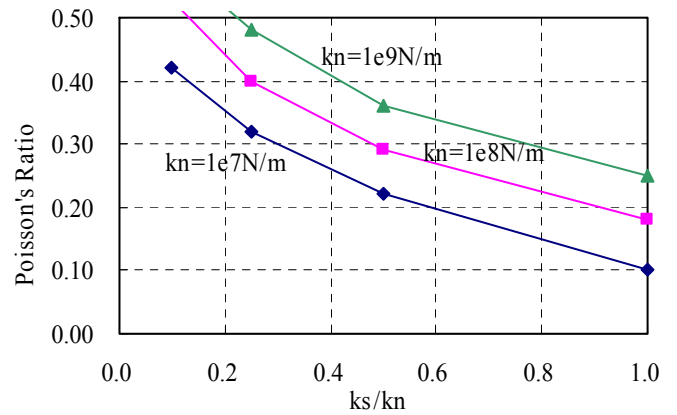Figure 5.2.3 Young's Modulus vs ks/kn ($\sigma 3$=100kPa)

Figure 5.2.4 Poisson's ratio vs ks/kn ($\sigma 3$=100kPa)

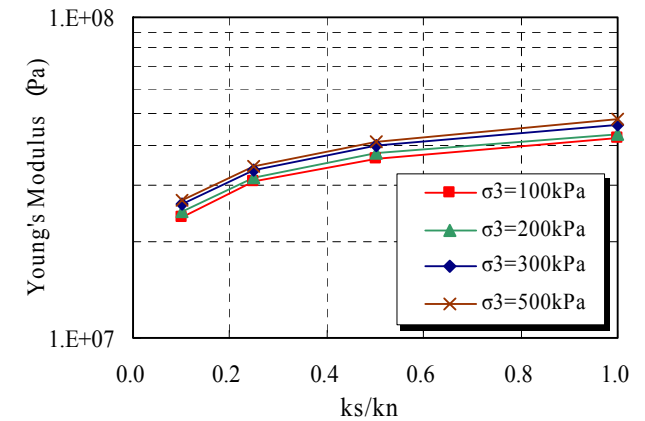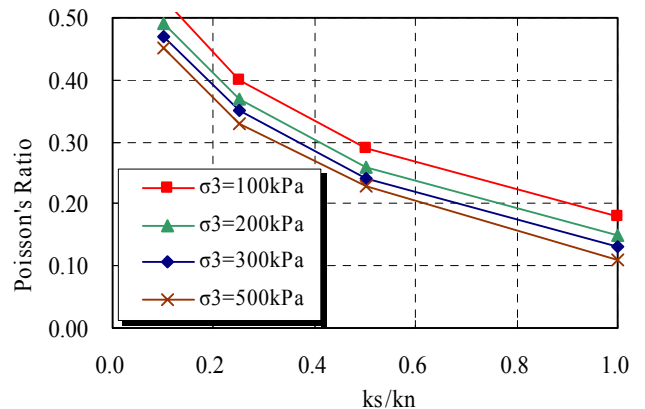
Figure 5.2.5 Young's Modulus vs ks/kn (kn=1e8N/m)

Figure5.2. 6 Poisson's ratio vs ks/kn (kn=1e8N/m)
Failure strength

In order to examine the failure strength of rubble assembly, a series of biaxial calculations test under several particle friction coefficients were performed. After the isotropic stress state is obtained under the specified particle friction coefficient as initial condition, axial constant strain is loaded by the upper and the bottom wall. In the shearing process, the movements of the lateral wall are controlled to keep constant confining pressure; the peak strength of the specimen is obtained as a result. In this simulation, the friction between two particles is taken into account in the model of the Coulomb law.

Figure 5.2.7 shows the correlation between obtained peak friction angle and given particle friction coefficient when the normal stiffness kn is 1e8(N/m) and the ratio ks/kn is 0.25. Regarding the particle friction angle of the materials, the peak strength did not increase even though high particle friction coefficient was used. It is clear that the model is using only circular particles, and then the sample can not reach high strength. It seems to need to use non circular element if high strength should be required.

Figure 5.2.8 shows relationship between the axial deviatoric stress and the axial strain with difference confining pressure when the ratio kn/kn is 0.25 and the particle friction coefficient is 1.5. The axial deviatoric stress increases when the confining pressure increases. This behaviour is similar to the result in triaxial test for real rubble grains.

Regarding dilation, the correlations between the volumetric strain and the axial strain are shown as figure 9. Volumetric expansion during shearing process is greater for the specimen that is in case of low confining pressure.

Effect of particle stiffness on Failure strength

Figure 5.2.10 to 13 show the correlation between the axial strain for the volumetric strain and the axial deviatoric stress respectively when the ratio ks/kn are 0.1,1.0 and particle friction confident are 0.5,1.0.

As the ratio ks/kn is smaller, volumetric expansion due to dilatancy is greater with same particle friction coefficient. This phenomenon means that the specimen with low ratio of ks/kn is easy to slip and deform to the shearing direction. As a result ,the volumetric strain due to shear increases.

Regarding axial deviatoric stress, in case of low confining pressure, the peak strength does not affected by the ratio ks/kn. However, in case of high confining pressure, as the ratio ks/kn increases, the strength of the specimen also increases with the same particle friction coefficient. From the these results, the tendency of the ratio ks/kn is that when the ratio ks/kn is large, the dilation is small and the strength is high.
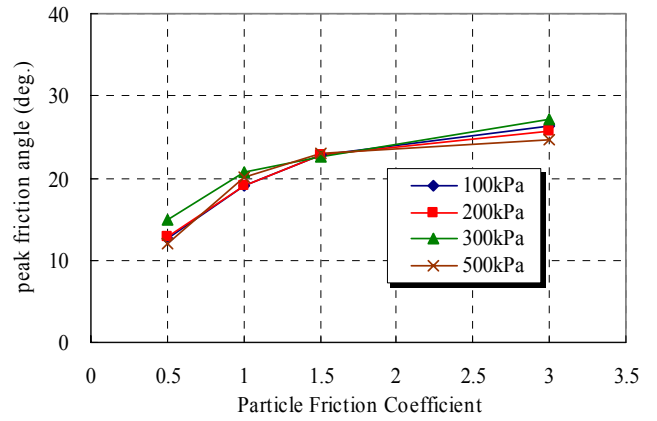

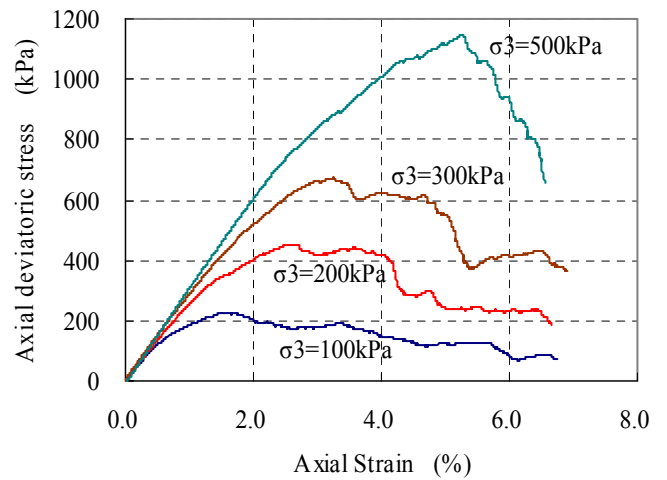Figure 5.2.7 Peak friction angle vs particle friction coefficient

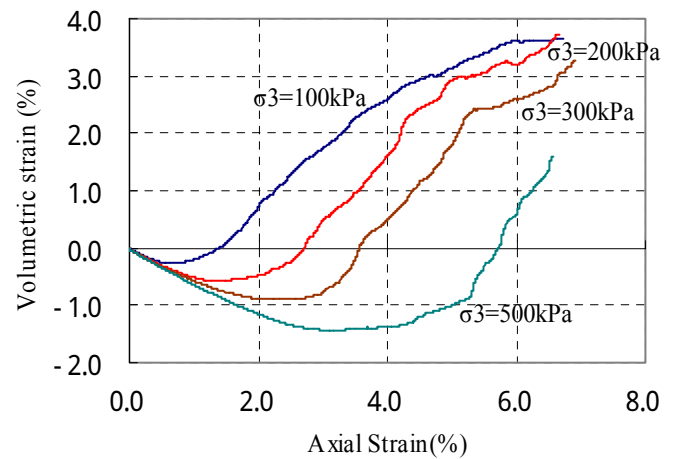Figure 5.2.8 Axial deviatric stress vs axial strain : ks/kn=0.25

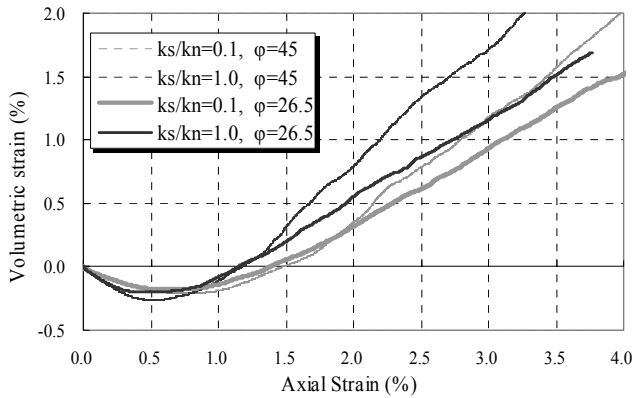
Figure 5.2.9 Volumetric strain vs axial strain: ks/kn=0.25

Figure 5.2.10 Volumetric strain vs axial strain($\sigma 3$=100kPa)

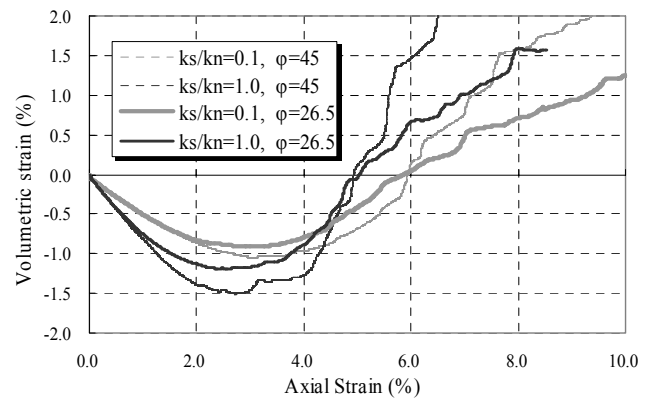Figure 5.2.12 Volumetric strain vs axial strain($\sigma 3$=500kPa)

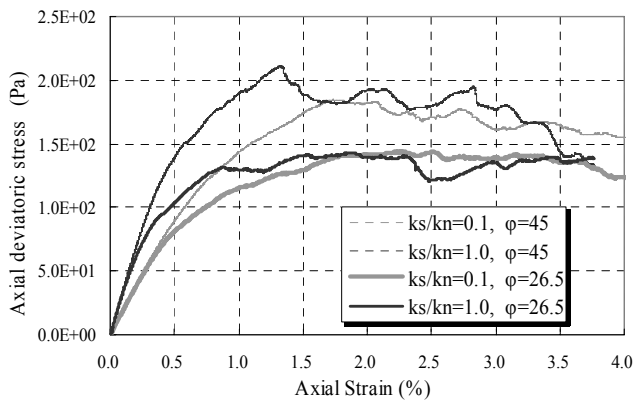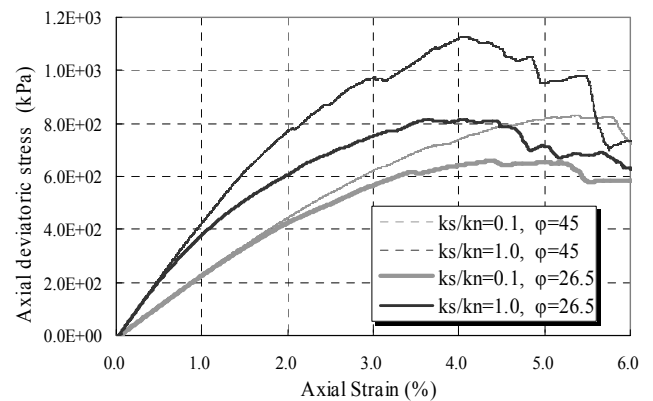Figure 5.2.11 Axial deviatric stress vs axial strain($\sigma 3$=100kPa)

Figure 5.2.13 Axial deviatric stress vs axial strain($\sigma 3$=500kPa)

5.2.4 CONCLUSION

The relationship between micro-properties as the DEM parameters and macro-properties as the parameters obtained in the laboratory was presented quantitatively using biaxial DEM simulations. Conclusive summary are described here as follows.

1) The normal stiffness of particles could be possible to estimate by Young's modulus of the real materials.
2) Poisson's ratio depends on the ratio ks/kn.
3) The effect of confining pressure to the normal stiffness of particles is small.
4) Poisson's ratio is affected by the confining pressure.
5) The strength as internal friction angle has a limit only by using only circular elements.
6) The ratio ks/kn is large, the dilation is small and the strength is high.

In this study, we limit to use 2-dimensional circular particles and dense packing model. Therefore it will be necessary to improve the rubble model using non-circular and non- sphere elements because high strength can not be expected only by circular elements.

REFERENCE

Cundall, P. A., and Strack, O. D. L. (1979). A discrete numerical model for granular assemblies', Géotechnique 29, No. 1, 47-65.

Miyata,M.,Sugano,T.,Mustoe,G.G.W.,Nakagawa,M.,Tanaka, T.(2001),Study on the Force Support System within a Rubble Rock Foundation using Discrete Element Method,ICADD-4,267-270

Kobayashi, M., Terashi, M., Takahashi, K. (1987) Bearing Capacity of a Rubble Mound Supporting a Gravity Structure, Rept. of PHRI vol. 26, No.5

Ishikawa, T., Sunaga, M., Domg, J., Namura, A.(1997) Cyclic Deformation Characteristics of Railroad Ballast in Triaxial Tests, Journals of the Japan Society of Civil Engineers. No.575,pp169-178 (in Japanese)

Potyondy, D.(2002) A Bonded-Disk Model for Rock:Relating Microproperties and Macroproperties, Discrete Element Methods Numerical Modeling of Discontinua, 340-343.

Itasca Consulting Group, Inc. 2003, PFC3D – Particle Flow Code in 3 Dimensions, Version 3.0 User's Manuals. Minneapolis: Itasca.

5.3 EFFECT OF PARTICLE PROPERTY ON MECHANICAL BEHAVIOUR OF RAILROAD BALLAST IN DISCONTINUOUS ANALYSIS

5.3.1 INTRODUCTION

The study of "Track deterioration" is one of the principal assignments in railway engineering because track deterioration has serious consequences on the safety of train operation. Track deterioration observed mainly at ballasted tracks is a phenomenon such that the rail level at train passages is irregular toward the longitudinal direction of railway track with repeated train passages. Incidentally, the ballasted track structures are composed of rails, sleepers, railroad ballast and roadbed as shown in Figure 1. The railroad ballast component in which sleepers are embedded is a pile of well-compacted crushed stones. The mechanism of track deterioration is being researched in many countries. In general, a dominant factor of track deterioration is supposed to be uneven subsidence of railroad ballast caused by cyclic wheel loading. Nevertheless, there are a number of points uncertain in the mechanism of track deterioration at the present stage. The reason for this is that the properties of the substructure components consisting of railroad ballast and roadbed are much more variable and complicated than those of the superstructure components consisting of rails, fasteners and sleepers. Therefore, it is essential to examine the cumulative irreversible (plastic) deformation characteristics of railroad ballast in detail.
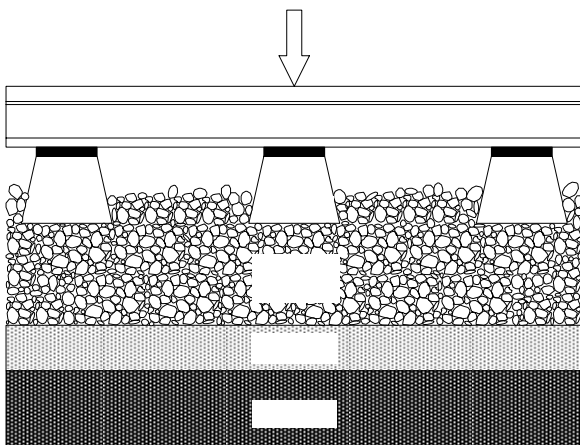

Figure 5.3.1 Ballasted track structure

The railroad ballast is usually composed of single-grained crushed andesite stone, namely "ballast." Traditionally, angular, crushed, hard stones and rocks, uniformly graded and free of dust and dirt, have been considered good ballast materials because such ballast can bear high contact pressures from a sleeper at train passages over a long period of time. Besides, the mechanical behaviour of railroad ballast can be characterized by the in-situ laminated state of ballast particles such as density and thickness of ballast layer, namely "ballast depth." The reason why both

the particle properties of individual ballast particles and their in-situ laminated state influence the deformation characteristics of railroad ballast is that complex behaviours of railroad ballast are caused by the movement of ballast particles from the viewpoint of the mechanics of granular materials. The results of full-scale track tests (Ishikawa et al, 1999) supported that the movement of ballast particles, accompanied by the fabric transformation of particle alignment, influenced the cyclic plastic deformation characteristics of railroad ballast strongly. To sum up, the mobility of individual ballast particles seems to be concerned with the mechanical properties of railroad ballast.

The conventional analytical model composed by the mass - elastic spring - dashpot system like Figure 2 cannot evaluate the non-uniform fabric transformation of particle alignment within railroad ballast which originates in the movement of ballast particles. Accordingly, the mechanical properties of ballast, even though they have a major influence on the mechanism of track deterioration, have been given much less consideration so far. Therefore, a new method for analyzing track deterioration, which can evaluate the movement of ballast particles sufficiently, should be developed in order to improve the reliability of analytical results and rationalize the design method of ballasted track. Discontinuous analysis seems to be effective in simulating the mechanical behaviour of railroad ballast because it regards a ballast particle as an element of discontinuous analysis. However, the precision of numerical simulations with discontinuous analyses seriously depends on how to model imhomogeneous internal structure of granular materials.
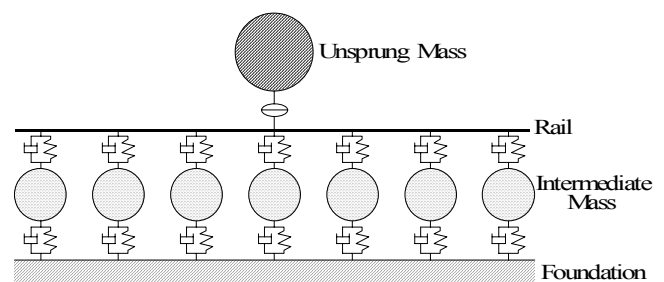

Figure 5.3.2 Mass-spring model in conventional theory of track deterioration.

This section describes a fundamental study to improve the reliability of discontinuous analysis more than the conventional mass-spring model by evaluating the mobility of individual particles in terms of the mechanics of granular materials. Accordingly, the numerical simulations of bearing capacity tests for ballasted track were performed with discontinuous analysis regarding a ballast particle as a regular or an irregular polygon block (the term "block" is used here in the same way as the term "element"). The following assignments are discussed by comparing model tests of ballasted track with the numerical simulations;

- To evaluate the influence of the particle properties such as particle shape and grain size distribution on the mechanical behaviour of railroad ballast in bearing capacity test of ballasted track with discontinuous analysis.
- To examine the validity and limit in modelling methods of railroad ballast with two-dimensional discontinuous analysis comparing the real mechanical behaviour of railroad ballast with analytical results.

5.3.2 ANALYTICAL METHODS

Modelling

The simulations of bearing capacity tests for model ballasted track (Ishikawa and Sekine, 2002) were performed with two-dimensional DDA models. The Discontinuous Deformation Analysis (DDA, proposed by Shi and Goodman, 1985) is a kind of discontinuous analysis. In DDA, each block is separated by its boundaries and moves individually. DDA is based on the principle of minimum potential energy like FEM (Finite Element Method), however DDA is different from FEM in that DDA is based on discontinuum mechanics like DEM (Distinct Element Method).

Figure 5.3.3 shows the size, dimension and boundary condition of analytical model tracks, which simulates a one-fifth scale model of a full-scale track. However, for bearing capacity tests, both the analytical model and the real model tracks have a single aluminum sleeper and no rail. The analytical model, which simulates a longitudinal section of the ballasted track, is in the plane strain state with the longitudinal section assumed to infinitely continue like the real model track. Figure 5.3.4 shows the element meshes of DDA models before loading. The DDA model is composed of some polygon blocks, named "ballast blocks," which represent andesite ballast particles and rectangular blocks, named "a sleeper block" which represents a aluminum sleeper, named "a roadbed block" which represents steel roadbed and named "side blocks" which represent a rigid soil container.
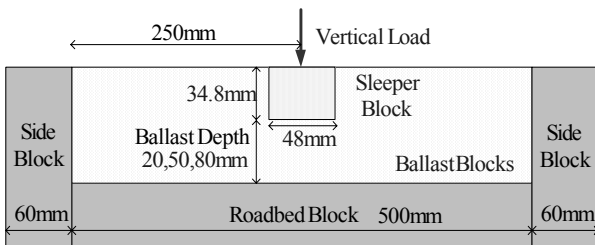

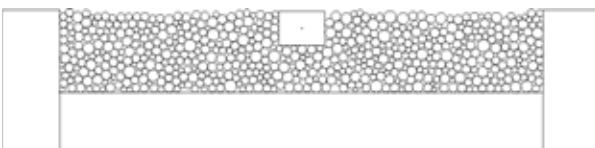Figure 5.3.3 Schematic section of DDA model

Figure 5.3.4a Element mesh (ballast depth 50mm, A ballast, regular icosagon)
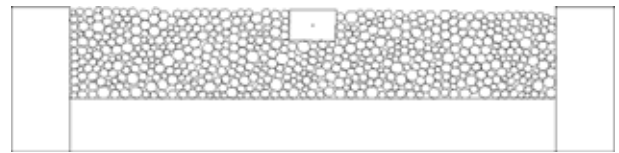

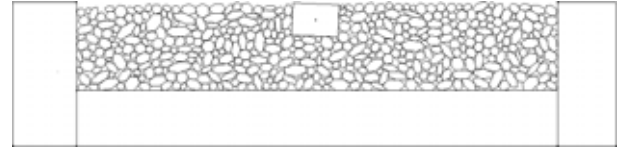Figure 5.3.4b Element mesh (ballast depth 50mm, A ballast, regular hexagon)

Figure 5.3.4c Element mesh (ballast depth 50mm, A ballast, expanded hexagon)
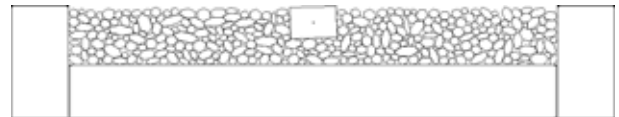

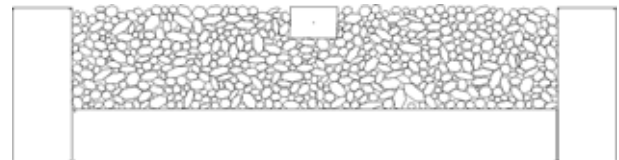Figure 5.3.4d Element mesh (ballast depth 20mm, A ballast, expanded hexagon)

Figure 5.3.4e Element mesh (ballast depth 80mm, A ballast, expanded hexagon)

Most important point in numerical modelling with discontinuous analysis is how to model the assemblage of ballast particles having a variety of particle shapes and grain sizes. According to the experimental results (Kohata et al., 1999), the stress-strain behaviour of granular materials is strongly influenced by grain size distribution and particle shape. Therefore, in the simulations, two types of grain size distribution and three types of particle shape are employed in order to model the assemblage of ballast particles.

Figure 5.3.5 shows the gradation curves for railroad ballast of DDA models, together with their mean grain sizes D_{50} and uniformity coefficients U_c. Two types of model ballast which had different mean grain size from each other were employed in this study. The proper grading of railroad ballast provided by the Japanese railway specification has a grain size distribution between approximately 60 mm and 10 mm. Both types of ballast have one-fifth mean grain size distribution of real railroad ballast and the grain size distribution similar to the proper grading of real railroad ballast. The term "A ballast" is used to refer to the model ballast which uniformity coefficient is smaller, and the term "B ballast" is used to refer to the other.

Figure 5.3.6 shows the classification of particle shape for real ballast particles with the method proposed by Zigg, 1935. It indicates that even though at the same grain size, the shape of ballast particles is various. In general, the shape of individual particles

is characterized by the indexes of angularity and sphericity. In the simulations, three types of the element shape, regular icosagon, regular hexagon and expanded hexagon, are employed for a ballast block in view of the shape of actual ballast particles. Here, an expanded hexagon block is made by extending a regular hexagon block in consideration for the dispersion in the shape of real ballast particles as shown in Figure 5.3.6. The aspect ratio of an expanded hexagon block was selected at random from the distribution of aspect ratios for the sieve mesh close to diameter of the original hexagon block. In this study, the effect of the angularity on the mechanical behaviour of numerical models is evaluated by the difference in bearing capacity between models using regular icosagon blocks and regular hexagon blocks, and the sphericity is evaluated by the difference between models using regular and irregular hexagon blocks.
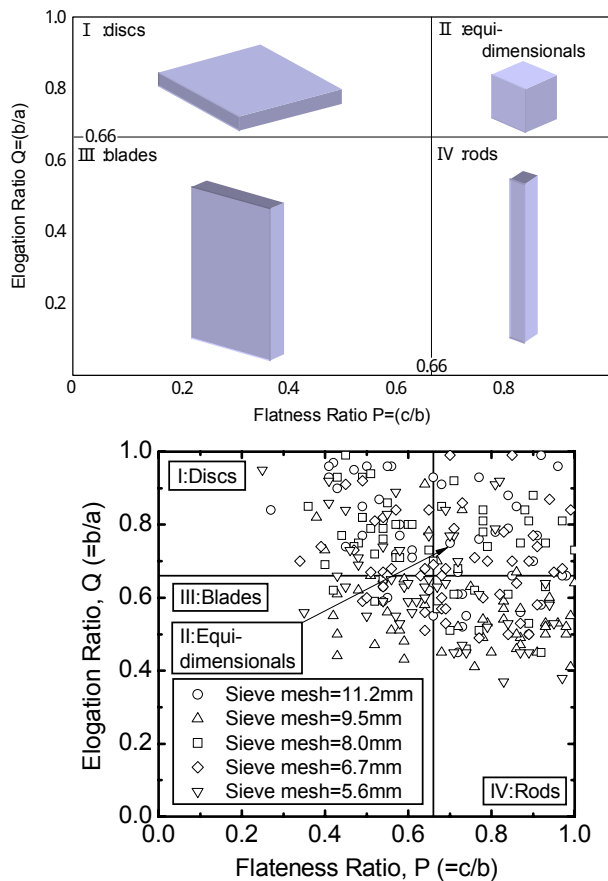

Figure 5.3.5 Classification of particle shape for ballast particles with the method proposed by Zigg, 1935
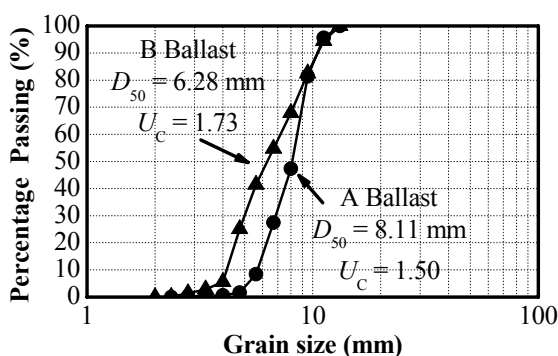

Figure 5.3.6 Grain size distribution of ballast blocks

Railroad ballast of DDA models were made with the above-mentioned six types of ballast blocks as follows. First, ballast blocks were thrown one by one into a frame of track profiles to model the random particle alignment in real railroad ballast. After filling the frame with ballast blocks, the frame was removed. Second, a stability analysis was done by gravity force of 1.0 G. In this study, the state of DDA models after stability analysis is called "the initial loading state". Figure 5.3.4 shows the initial loading state of each model. Here, three type of ballast depth, 20mm, 50mm and 80 mm, are employed. Accordingly, in the simulations, eighteen types of analytical model which differ in particle shape of a ballast block, grain size distribution of ballast blocks and ballast depth were employed as shown in Figure 5.3.4.

Table 5.3.1 shows the feature of DDA models in comparison with experimental conditions. Seeing Table 5.3.1, it is recognized that for the same ballast depth and particle shape the total number of ballast blocks for DDA models of A ballast is smaller than that for DDA models of B ballast, and that for the same ballast depth and grain size distribution the total number of ballast blocks increases in order of regular icosagon, regular hexagon and expanded hexagon. In the meantime, the porosity of DDA models is much smaller than that of experiments as shown in Table 5.3.1, though there is little difference in the porosity among all analytical models. This phenomenon seems to be mainly caused by the reason that the DDA models used in this study are two-dimensional while the laminated state of experimental specimens is three-dimensional.

Analytical Conditions

DDA analyses were performed with two-dimensional models using linear elastic blocks with plane strain. Table 5.3.2 shows the material properties of blocks and the interface properties of block edges. In this study, when two DDA blocks come in contact, springs and a slider are created at contact points as shown in Figure 5.3.7. Accordingly, the analytical input parameters of DDA blocks are characterized by the material properties of a block, namely unit mass (γ), Young's modulus (E) and Poisson's ratio (ν), and the interface properties of block edges, namely block friction angle (ϕ_μ) and cohesion of surface (C_μ). As for the material properties, the parameters were set by referring to the design values and past experimental results. On the other hand, the interface properties were set as follows. First, the block friction angle (ϕ_μ) between ballast blocks was set equal to 55º because the internal friction angle derived from the analytical results in the case of ϕ_μ=55º indicated the best fit to experimental results in simulating triaxial tests with DDA (Ishikawa et al, 1997). As for ϕ_μ between a ballast block and other kinds of blocks, the value was set equal to 37º by

Table5.3.1 Features of DDA models

Model		A ballast			B ballast		
		Number of Ballast Blocks	Porosity n(%)	Density (tm^{-3})	Number of Ballast Blocks	Porosity n(%)	Density (tm^{-3})
ballast	regular icosagon	465	20.1	2.16	610	18.4	2.20
depth	regular hexagon	445	18.7	2.20	552	18.3	2.21
20mm	expanded hexagon	318	21.8	2.11	389	17.5	2.23
	experiment	-	48.2	1.40	-	-	-
ballast	regular icosagon	610	19.0	2.19	913	17.7	2.22
depth	regular hexagon	598	20.1	2.16	853	18.3	2.21
50mm	expanded hexagon	451	21.4	2.12	552	16.9	2.24
	experiment	-	46.0	1.46	-	-	-
ballast	regular icosagon	803	18.5	2.20	1153	17.5	2.23
depth	regular hexagon	751	18.5	2.20	1061	16.7	2.25
80mm	expanded hexagon	548	21.0	2.13	718	16.3	2.26
	experiment	-	46.3	1.45	-	-	-

Table5.3.2 Material properties of analytical model

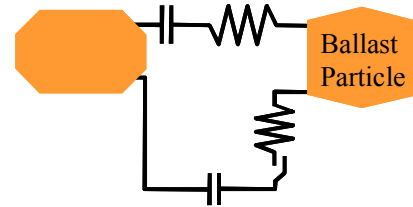| Property	Sleeper	Ballast	Roadbed	Side
Unit Mass γ	2.7tm^{-3}	2.7tm^{-3}	7.8tm^{-3}	7.8tm^{-3}
Young's Modulus E	70GPa	20GPa	210.0GPa	210.0GPa
Poisson's Ratio ν	0.3	0.1	0.3	0.3
Cohesion C_μ	0	0	0	0
Friction Angle ϕ_μ	37.0°	55.0°	37.0°	37.0

Figure 5.3.7 Contact mechanism between DDA blocks

referring to conventional studies. Besides, as for C_μ between all materials, the value was set equal to zero by considering that ballast is a coarse granular material.

Vertical load was applied to DDA models in the initial loading state. The loading point was the centre point of the sleeper block as shown in Figure 5.3.3. Vertical load slowly increased from 0 kN to 5 kN at the constant loading speed which was regarded as static loading like the real experimental condition. Assuming P=5kN a load to act on a single rail, it corresponds to a simulated wheel load of 194 kN (fn. the track modulus C=100MN/m^2, dynamic load factor S=1.5, rail type: 50N, sleeper type: PC3 and tie spacing 600mm) when calculated by applying the theory of elasticity in consideration of track rigidity. Furthermore, the gravity force was applied to DDA models throughout the simulation.

5.3.3 RESULTS AND DISCUSSION

Load–Displacement Relations

Figure 5.3.8 and Figure 5.3.9 show the relations of the sleeper block between the vertical load P and the vertical displacement u at the centre of gravity of the sleeper block derived from the bearing capacity test simulations. Figure 5.3.8 shows the load-displacement relations for DDA models using A ballast at the respective ballast depths of 20mm, 50mm and 80mm comparing three types of the element shape, and the relations for DDA models using B ballast are shown in Figure 5.3.9. These figures also compare

analytical results with experimental results. In this study, the bearing capacity of DDA models can be defined as the vertical displacement at P=5kN. It is considered that the DDA model has stronger bearing capacity in case of obtaining smaller vertical displacement at P=5kN.

First, the influence of the particle properties of ballast blocks on the bearing capacity of ballasted track is examined. At the beginning, discussed is the difference in the load-displacement relations due to the difference in the particle shape of a ballast block. Comparing analytical results of each model at the same ballast depth in Figure 5.3.8, the bearing capacities of DDA models for A ballast decrease in order of expanded hexagon, regular hexagon, and regular icosagon. Also, with increasing the total number of ballast blocks, the bearing capacity decreases as can be seen when comparing Table 5.3.1 and Figure 5.3.8. The same is true for analytical results of B ballast as shown in Figure 5.3.9. These results indicate that the difference in the particle shape of a ballast block has a considerable influence on the bearing capacity of DDA models.

Furthermore, Figure 5.3.10 compares the vertical displacement at P=5kN derived from analytical results of each DDA models. In Figure 5.3.10, though the bearing capacity of DDA model using regular icosagon blocks is much smaller than analytical results using expanded hexagon blocks or regular hexagon blocks, the bearing capacities in case of expanded hexagon blocks and regular hexagon blocks are approximately
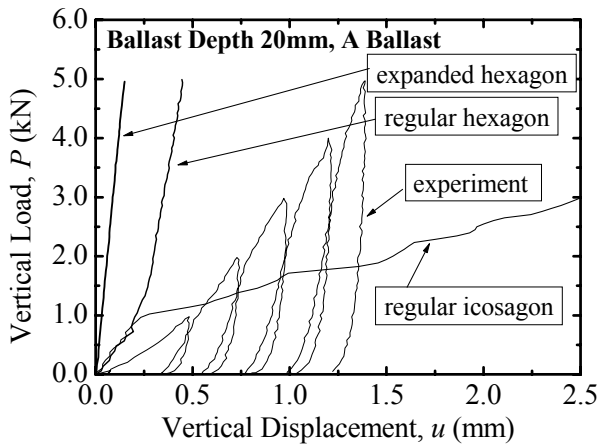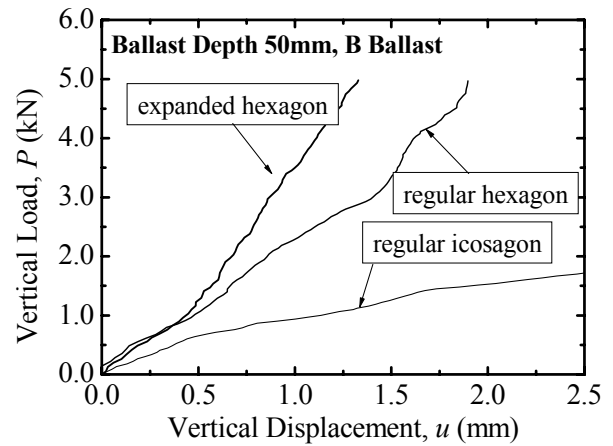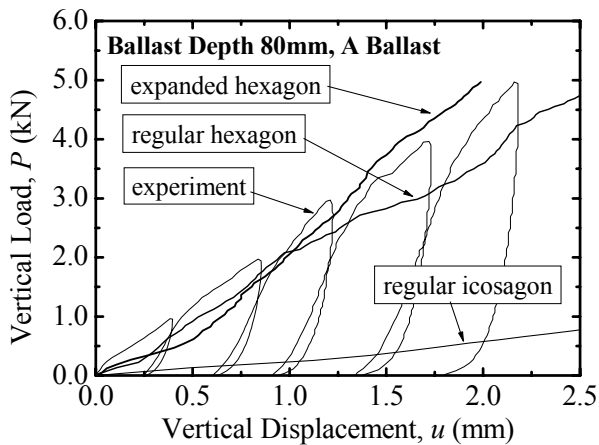
(a) Ballast depth 20mm
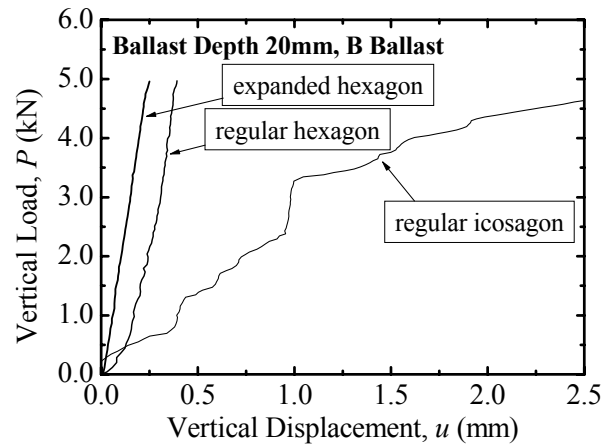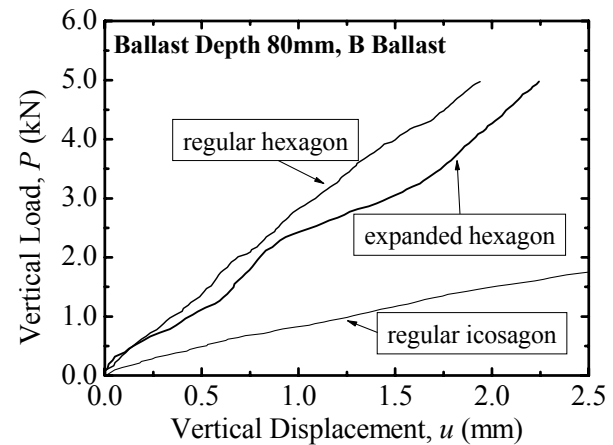

(a) Ballast depth 20mm
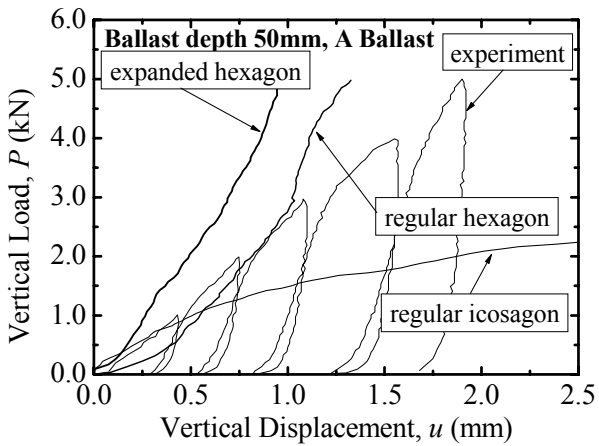
(b) Ballast depth 50mm

(b) Ballast depth 50mm

(c) Ballast depth 80mm

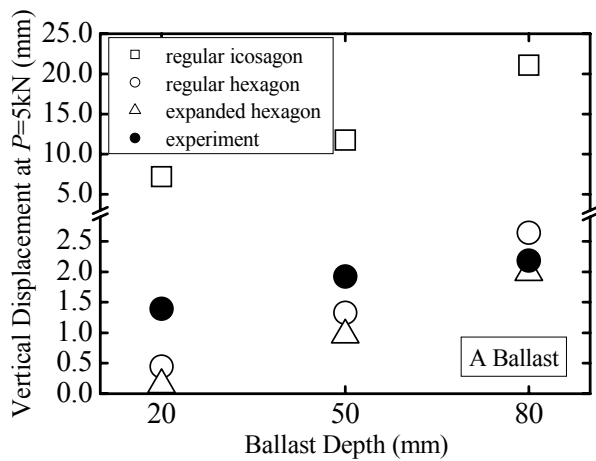Figure 5.3.8 Load – displacement relations (A ballast)

(c) Ballast depth 80mm

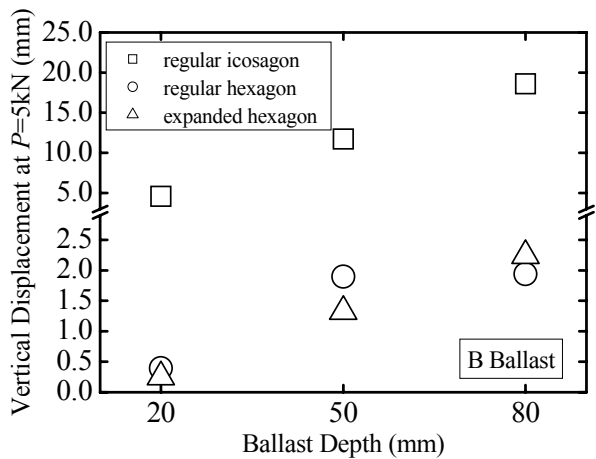Figure 5.3.9 Load – displacement relations (B ballast)

the same, regardless of grain size distribution and ballast depth. In terms of the mechanics of granular materials, the difference between expanded hexagon blocks and regular hexagon blocks is the sphericity of DDA blocks, while the difference between regular hexagon blocks and regular icosagon blocks is the angularity of DDA blocks. Accordingly, these results indicate that the angularity of ballast blocks has a greater effect on the bearing capacity of railroad ballast in discontinuous analysis than the sphericity.

Next, discussed is the difference in the load - displacement relations due to the difference in the grain size distributions of model ballast. Comparing Figure 8 with Figure 5.3.9 at respective particle shapes of a ballast block under the same ballast depth condition, in case of DDA model using regular icosagon, the bearing capacity of DDA models for A ballast is larger than that for B ballast. However, in case of the other shapes, the clear tendency cannot be recognized. These results indicate that the difference in the grain size distributions of model ballast has a little influence on the bearing capacity of railroad ballast in discontinuous analysis compared with the influence of particle shape. The same is true for Figure 5.3.10.

5-14

(a) A ballast

(b) B ballast

Figure 5.3.10 Comparison of bearing capacity

Second, the validity of modelling methods of railroad ballast is verified. At the beginning, discussed is the difference in the load-displacement relations due to the difference in the particle shape of a ballast block. Comparing analytical results with experimental results at the same ballast depth in Figure 5.3.8, it is recognized that the load-displacement relations of DDA model using regular icosagon blocks has much smaller stiffness than experimental results. While, the load-displacement relations of DDA model using expanded hexagon or regular hexagon blocks resembles experimental results for A ballast at every ballast depth. Moreover, Figure 5.3.10a compares the vertical displacement at P=5kN of each DDA models with experimental results. In Figure 5.3.10, though the bearing capacity of DDA model using regular icosagon blocks is much smaller than that of experimental results, the bearing capacity of DDA model using expanded hexagon blocks or regular hexagon blocks is approximately equal to experimental results at every ballast depth. From these results, it is considered that the usage of expanded hexagon or regular hexagon blocks is appropriate of simulating the mechanical behaviour of railroad ballast with DDA. It is said that a ballast particle has at most six distinctive angles (Kono et al, 2000). Accordingly, the expanded hexagon blocks imitate the shape of real

ballast particles well in terms of the angularity and the sphericity. It is interesting that the above-mentioned results were obtained, and this indicates that the imitation of the shape of real ballast particles makes the reliability of analytical results improved.

Mechanical Behaviour of Railroad Ballast

First, the influence of the particle shape of ballast blocks on the mechanical behaviour of railroad ballast is examined. Figure 5.3.11 shows the distribution of principal stress for DDA blocks at P=5kN. In Figure 5.3.11, it is recognized that the analytical results of DDA models using regular icosagon blocks differ from those of DDA models using expanded hexagon in the distribution of principal stress. For example, comparing Figure 5.3.11c with Figure 5.3.11d, in case of regular icosagon, there are many ballast blocks underneath the sleeper block which principal stress turns toward horizontal direction. Whereas, in case of expanded hexagon blocks, the principal stress of the ballast blocks mainly turns toward vertical direction. Besides, in Figure 5.3.11d, it can be observed that high principal stress appears underneath the sleeper block. However, principal stress observed in Figure 5.3.11c is smaller compared with Figure 5.3.11d on the whole. The reason for this is that the DDA model using regular icosagon blocks cannot sustain vertical loads by the ballast blocks under the sleeper block alone as it has very low bearing capacity, though DDA models using expanded hexagon blocks can sustain it due to their high bearing capacity. Consequently, the lateral flow occurs in railroad ballast around the sleeper block in Figure 5.3.11c, and it leads to large settlement of the sleeper block. These results indicate that the particle shape of a ballast block is one of the dominant factors to determine the mechanical behaviour of railroad ballast in numerical simulations, and that the mobility of individual particles is concerned with the mechanical properties of railroad ballast.

Second, the influence of ballast depth on the mechanical behaviour of railroad ballast in discontinuous analysis is examined. Comparing Figure 5.3.11d with Figure 5.3.11b, it is recognized that in case of ballast depth of 80 mm, high ballast pressure suffered from a sleeper at train passages gradually spreads inside railroad ballast with the increment of ballast depth, though, in case of ballast depth of 20 mm, it does not spread well. These tendencies are in fair agreement with the experimental results. This indicates that discontinuous analysis is an effective method to simulate the mechanical behaviour of railroad ballast in bearing capacity tests if an element of discontinuous analysis imitates the shape of real ballast particles well.
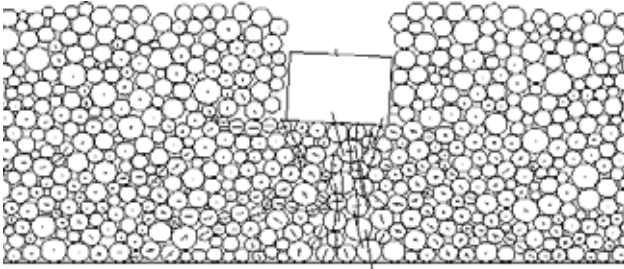
However, there is room for further investigation on the method to simulate the mechanical behavior of railroad ballast with two-dimensional discontinuous analysis. For example, according to Figure 8, though
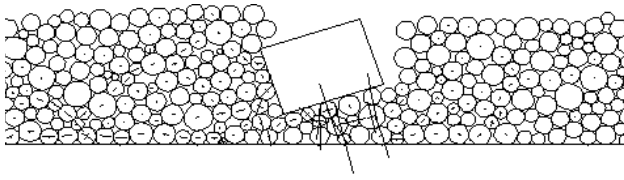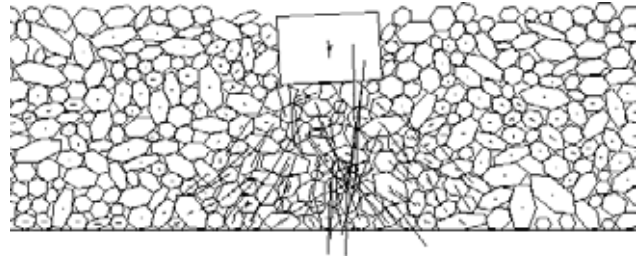
(a) Ballast depth 20mm, regular icosagon

(b) Ballast depth 20mm, expanded hexagon

(c) Ballast depth 80mm, regular icosagon

(d) Ballast depth 80mm, expanded hexagon

Figure 5.3.11 Distribution of principal stress

in case of the ballast depth of 50mm or 80 mm the load-displacement relations of analytical results (seeing the relations of expanded hexagon or regular hexagon) agree well with experimental results, in case of the ballast depth of 20 mm the analytical results have much harder stiffness than experimental results. This phenomenon seems to be mainly caused by the reason that the DDA models used in this study are two-dimensional while the laminated state of experimental specimens is three-dimensional. In case the total number of ballast blocks is small, it is considered that a problem in modelling real phenomenon with two-dimensional analysis tends to become evident as free motion of individual particles is strongly restricted.

5.3.4 CONCLUSION

The following conclusions can be derived from the results of a series of numerical simulations that regard a ballast particle as a regular or an irregular polygon and the comparison of experimental results for model ballasted track and the numerical simulations;
(1) Discontinuous analysis is an effective method to simulate the mechanical behaviour of railroad ballast in bearing capacity tests, and the imitation of the shape of real ballast particles makes the reliability of analytical results improved.
(2) In discontinuous analysis, the difference in the particle shape of a ballast block has a greater influence on the bearing capacity of railroad ballast than the grain size distributions of model ballast. Especially, the angularity of a ballast block has a considerable influence on the bearing capacity of railroad ballast, compared with the sphericity.

(3) The particle shape of a ballast block is one of the dominant factors to determine the mechanical behaviour of railroad ballast in numerical simulations, and the mobility of individual particles is concerned with the mechanical properties of railroad ballast.
(4) In case total number of ballast blocks is small, a problem in modelling real phenomenon with two-dimensional analysis tends to become evident as free motion of individual particles in numerical simulation is strongly restricted compared with the true motion.

From what has been mentioned above, it was revealed that in numerical simulation with discontinuous analysis, the particle properties of a constituent particle like particle shape and grain size strongly influences the mechanical behaviour of particle assemblage as well as the sedimentary state like density and anisotropy of particle alignment, and they condition the accuracy of numerical simulations. However, it is yet known to what extent the shape of a constituent particle and the fabric arrangement of particle assemblage catch the prototype faithfully in order to control computational error within the permission range from the viewpoint of practical designing. There is room for further investigation on the assignments how detailed information is needed to numerical modelling with discontinuous analysis and how the difference between model and prototype would affect the mechanical behaviour of granular materials.

REFERENCE

Ishikawa, T., Kamon, M. and Namura, A., (1999). Experimental and analytical studies on the cyclic deformation characteristics of railroad ballast, Proceedings of IS Torino99, 783-792.

Ishikawa, T., Ohnishi, Y. and Namura, A. (1997). DDA applied to deformation analysis of coarse granular materials (ballast). Proceedings of ICADD-2, 253-262.

Ishikawa, T. and Sekine, E. (2002). Effects of Moving Wheel Load on Cyclic Deformation of Railroad Ballast. Proceedings of Railway Engineering-2002.

Kohata, Y., Jiang G.L. and Sekine, E. (1999). Deformation characteristics of railroad ballast as observed in cyclic triaxial tests. Poster Session Proceedings of the 11th Asian Regional Conference on Soil Mechanics and Geotechnical Engineering.

Kono, A., Sekine, E. and Kohata, Y. (2000). A study on shape evaluation method of granular material. Proceedings of the 5th International Symposium on Unbound Aggregates in Roads, 35-40.

Shi, G.H. and Goodman, R.E. (1985). Two dimensional discontinuous analysis. Int. J. Num. Anal. Methods. Geomech, 9: 541-556.

Zingg, T. (1935). Beitrag zur Schotteranalyse. Schweiz. Min. Petrol. Mitt., 15, 39-140.

5.4 EXPERIMENTAL OBSERVATION AND DIRECT SIMULATION OF PARTICLE-FLUID SYSTEM

5.4.1 INTRODUCTION

The Mechanical behavior of particle-fluid system plays important role in various engineering problems; in the field of geotechnical engineering, such phenomena as boiling, piping and liquefaction are of this type. It is, however, substantially difficult to observe the internal behavior of such phenomena, and few visualization techniques are available. One of well known methods is that using X-ray technique [1] which envisages the inside of particle-fluid system by detecting the differences in material density. The X-ray technique has the advantage of being applicable to actual materials, i.e. sand particles and pore water, while it can not visualize the flow of pore water because of the homogeneity of its density. A new technique, LAT-PIV, combining LAT (Laser-Aided Tomography) [2][3][4] and PIV (Particle Image Velocimetry) [5], was developed for visualizing both movement of particles and fluid flow: LAT for 3-D movement of each particle, and PIV for velocity field of fluid. A drawback of this method is that crushed glass is to be used as particulate media instead of actual geomaterials. The method, however, can treat digitalized images directly, which enables us to obtain higher resolution in the future with the progress in digital technology.

For simulating the fluid behavior in the particle-fluid system, such an averaging concept as Darcy's low is often employed. Recently direct simulation methods for the particle-fluid interaction have been developed in the scheme of FEM [6] and Lattice-Boltzmann Method [7]. This study also aims to develop a simulation method for the system using Smoothed Particle Hydrodynamics (SPH) [8][9] and Discrete Element Method (DEM). SPH, a meshless analysis method, has an advantage of avoiding mesh-discretization and re-meshing process. Moreover this method is expected to yield better simulation results because it employs Navier-Stokes equation. SPH and DEM are of the same nature in terms of the particle based formalism, thus they can be combined each other with comparative ease.

5.4.2 VISUALIZATION TECHNIQUE AND MEASUREING SYSTEM

Figure.5.4.1 shows a schematic illustration of the observation system used in this study. LAT, a kind of laser-slicing method, visualizes each particle motion including rotation inside a 3-D specimen composed of crushed glass and pore fluid which are of the same refractive index. PIV, also a kind of laser-slicing method, visualizes fluid motion by pursuing a pattern created by tracing powder mixed into the fluid. Simultaneous application of LAT to particle part and

PIV to fluid part enables us to observe the interaction of the particle-fluid system. A newly developed measuring system consists of a CCD monochrome camera (1 million pixels, 500 frames/sec) and a PC is able to take photographs in digitized form for almost 10 seconds with 500 fps as the marginal performance.
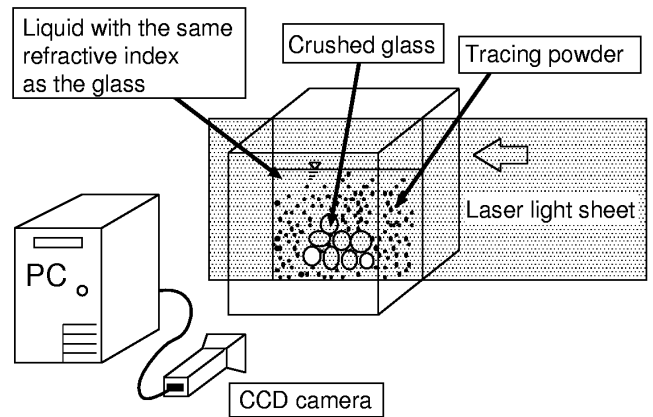
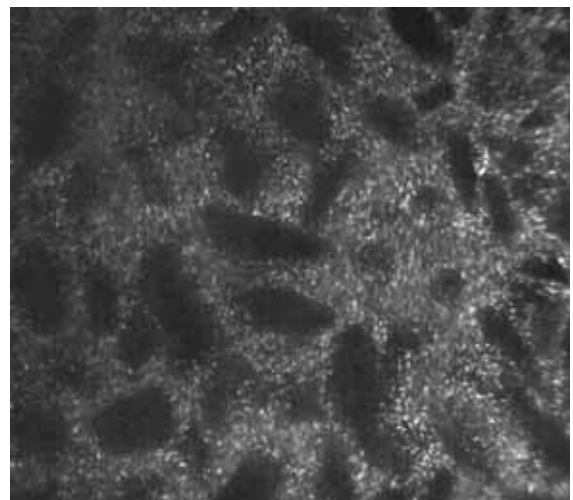

Fig.5.4.1 Brief overview of observation

Fig.5.4. 2   Snap shot by LAT-PIV.

Figure 5.4.2 shows a photograph taken by the LAT-PIV technique with numerous tracing powder (flecks) and cross sections of the glass grains (no pattern regions) on the laser light sheet. To separate the pore fluid area from the LAT-PIV image and improve the accuracy of image processing, fluorescent powder that gleams pale orange on the green laser sheet and green-cut filter were employed here.

5.4.3 VISUALIZATION OF PERMEABILITY TEST AND SEEPAGE FAILURE WITH LAT-PIV

In order to investigate the applicability of the LAT-PIV, a series of permeability tests including seepage failure was conducted. Crushed glass and silicone oil were adopted to compose specimens. The LAT-PIV requires the same refractive index between particles and pore fluid, which is attained by interblending two kinds of

silicone oil with different refractive indexes.
Figure 5.4.3 indicates a schematic diagram of the experimental apparatus and Table 1 lists the material properties.

The apparatus has a circulation loop for the silicone oil which flows upward from the bottom of the loosely packed specimen made by a pluviation method.

Wire mesh filters (1mm grid) placed close to the inlet zone are designed to avoid a local seepage failure caused by non- rectified inflow.
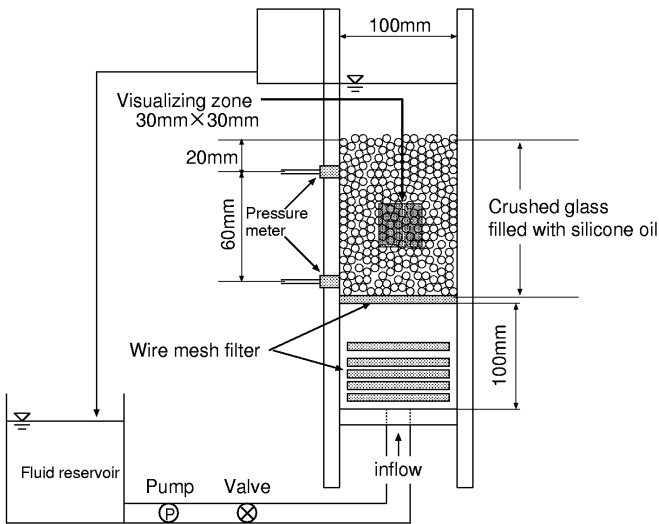
Fig.5.4.3 Schematic diagram of experimental

Table 5.4.1. Material properties

	Silicone oil	Glass grain	Tracing powder
Density	1.02 g/cm³	2.52 g/cm³	1.02 g/cm³
Diameter	---	2 ~ 5mm	40 μ m
Viscosity	20.6 mm²/s	---	---
Refractive index	1.514	1.514	---

The experimental procedures are as follows:
(1) Pump the silicone oil into the specimen by opening the valve, then keep the valve open to stabilize the outflow with a constant rate.
(2)After the stabilization, measure the pressure gradient and the mass of outflow.
(3)Visualize the interior of the specimen with the LAT-PIV during the steady state.
(4) Increase the flow rate slightly, and repeat the procedures (1) to (3) step by step.

The experiment comprised 20 stages from the seepage state to the boiling state with increasing flow rate. During the experiment, the laser light sheet always passed through 3cm inside the specimen with the same intensity and hundreds of cross-sectional digital images were taken at each stage.

5.4.4 RESULTS OF EXPERIMENT

Figure 4 plots the relationship between the mean fluid velocity and the hydraulic gradient obtained by the experiment. The data points are clearly divided into two regions: one corresponds to the seepage state (stage No. 0 - No.14) and the other to the boiling state (stage No.15 - No. 20).
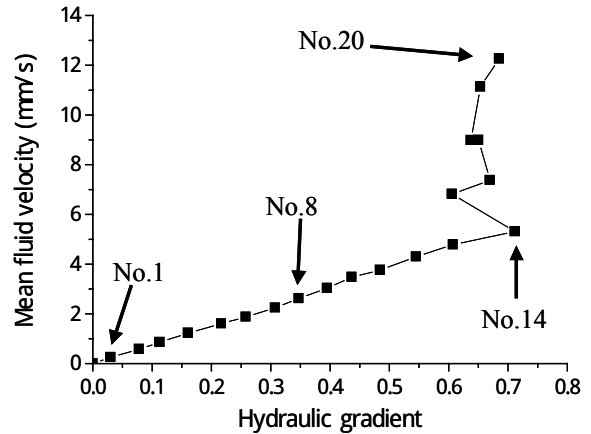
Fig.5.4.4.   Plot of mean fluid velocity vs. hydraulic gradient.

The value of critical hydraulic gradient is 0.71 at stage No. 14, which is comparative but a little smaller compared with the theoretical range from 0.78 to 0.92 corresponding to the maximum and the minimum void ratios, i.e. 0.90 and 0.59, respectively. In contrast to this result, the critical hydraulic gradient measured for another specimen made with bigger glass grains from 5 to 10 mm in diameter was definitely smaller than the theoretical range because of its high perviousness.

Within the stage from No. 0 to No. 14, a linear relationship exists between the mean fluid velocity and the hydraulic gradient, which represents the Darcy's law. The coefficient of permeability obtained from the slope of the line is 7.68×10^{-1} cm/s. In the field of geotechnical engineering, Hazen's equation or Taylor's equation are well known and often used for the estimation of permeability; the measured permeability was compared with that calculated by Ergun's equation [10]. The Ergun's equation, obtained on the assumption that the viscous losses and the kinetic energy losses are additive, covers the entire range of flow rates and is widely referred in chemical engineering. Since the Ergun's equation takes account of viscosity, density and porosity as well, it can be easily applicable to a special pore fluid like silicone oil. The Ergun's equation is given as follows:

$$i = \frac{150\mu(1-\varepsilon)^2}{\rho g(\phi d_m)^2 \varepsilon^3}v + \frac{1.75(1-\varepsilon)}{g(\phi d_m)\varepsilon^3}v^2$$

where the notations i and v indicate the hydraulic gradient and the mean fluid velocity; μ and ρ correspond to the viscosity and the density of the fluid; ε is the porosity and ϕ and d_m are spericity and diameter of the grains, respectively; g is the acceleration of gravity.

By substituting the values listed in Table 5.4.1 and the maximum porosity into this equation, then the the sphericity only remains uncertain for evaluating the hydraulic losses. According to the list of the sphericity [11] [12] , most kinds of grains often encountered in engineering fields are approximately within the range from 0.6 to 0.8: e.g. 0.65 for crushed glass, 0.83 for rounded sand. Figure 5 shows the relationship between the mean fluid velocity and the hydraulic gradient obtained from the Ergun's equation for different values of sphericity.

As can be seen in Fig. 5.4.5, when the sphericity equals to 0.704, the Ergun's equation yields a good agreement with the experimental result within the seepage stages. This value is, however, a little greater than the reference value of 0.65 for glass grains subjected to abrasion by means of ball milling.
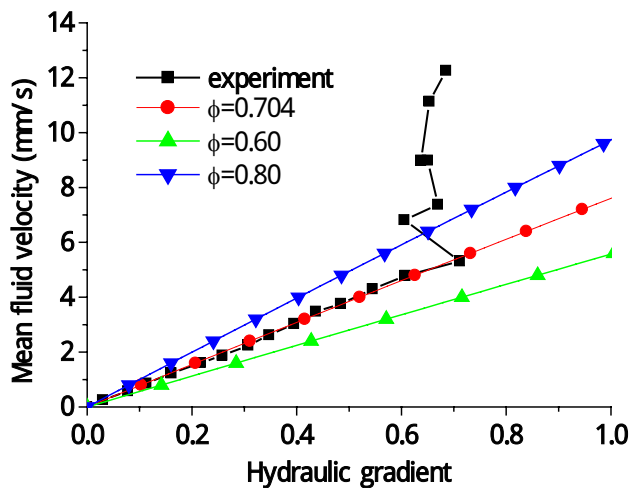The Ergun's equation gives the possible values of

Fig.5.4.5. Mean fluid velocity vs. hydraulic gradient with the fitting results of the Ergun's equation.

permeability bounded by the upper and the lower lines with triangle marks, which corresponds to the range from 5.53×10^{-1} cm/s to 9.76×10^{-1} cm/s. However, it is to be noted that the Ergun's equation can not predict the drastic change in the permeability due to boiling.

Figures 5.4.6, 7 and 8 represent the distributions of fluid velocity vectors inside the specimen at stage No.1, No.8 and No.14 indicated in Fig. 4, respectively.
To obtain these figures, a PIV image analysis with a sub-pixel accuracy was employed.
The magnifying power was set at 5.53×10^{-2} mm/pixel, and then 33 pixel (1.82mm) square template was used as a pattern matching area in the image analysis. The fluid velocity vectors were measured at 7885 points for each image with a lattice-like arrangement; the values of color indexes indicate the norms of the velocity vectors in terms of millimeter per second.
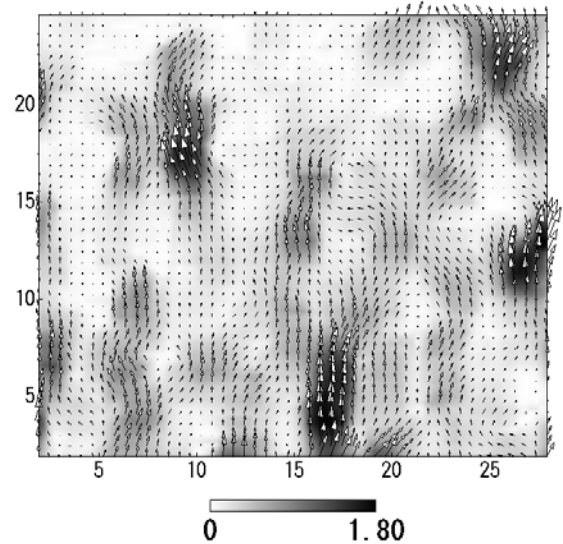Although these figures are found lacking in uniformity,

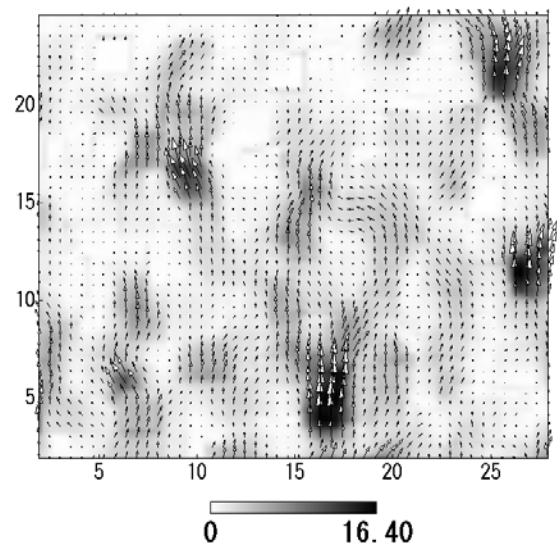Fig.5.4.6.   Distribution of fluid velocity at stage No.1,   60fps

Fig.5.4.7.   Distribution of fluid velocity at stage No.8,   250fps
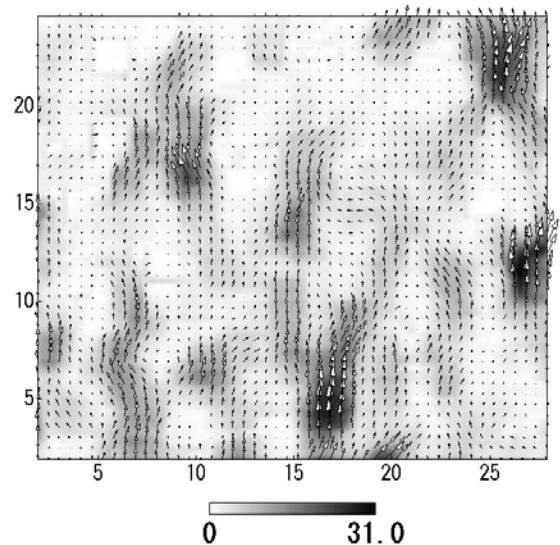

Fig.5.4.8.   Distribution of fluid velocity at stage No.14,   500fps

the region of faster flow always appears at almost similar spot at each stage within seepage state, which suggests an immutability of the pore structure.

Figure 5.4.9 shows the histograms of the vertical velocity components for stage No. 1, No. 8 and No. 14. The values on the horizontal axis stand for dimensionless vertical velocities normalized by the arithmetic averaged vertical velocity. The three lines for different stages coincide well and obviously indicate a non-Gaussian distribution with a long tail reaching to almost 8 on the horizontal axis. The measured distribution curves seem to be simulated by a log-normal distribution.

Since the velocity measurement using LAT-PIV technique provides a high resolution, such a non-Gaussian distribution is very useful in the Monte Carlo simulation often employed in modeling the long-term behavior of groundwater pollution.

Once exceeding the critical stage represented by No. 14, a quick condition or boiling occurred in the specimen, and the hydraulic gradient stayed fairly constant despite the increase in the inflow rate. Meanwhile the layer consisting of the glass grains was entirely destroyed by the hydrodynamic force; both the glass grain and the silicone oil started to move randomly. Two hundreds photographs were taken at stage No.20 with 500 fps (0.4 seconds in real time) and analyzed to clarify a complicate velocity field observed in boiling.

Figure 5.4.10 shows snapshots taken during the boiling together with the results of image analysis. As shown in those figures, the LAT-PIV successfully captured a time series of localized upward flow in the region of $20<x<25$. The change in the maximum vertical velocity component was traced from these images so as to characterize the flow state during boiling in terms of the Reynolds number.

In consequence, the Reynolds number calculated by the mean grain diameter, the fluid viscosity and the
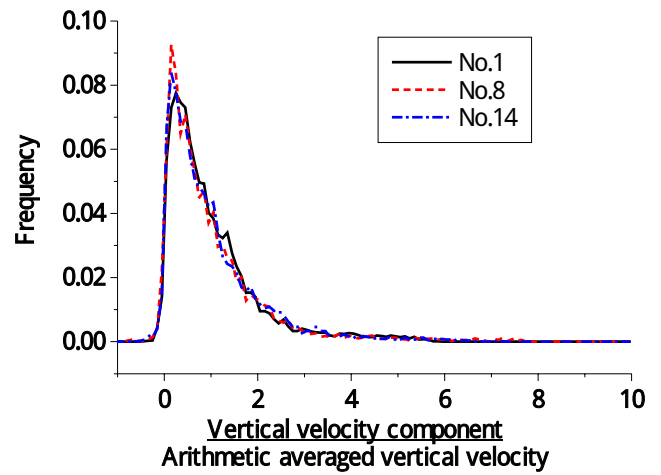

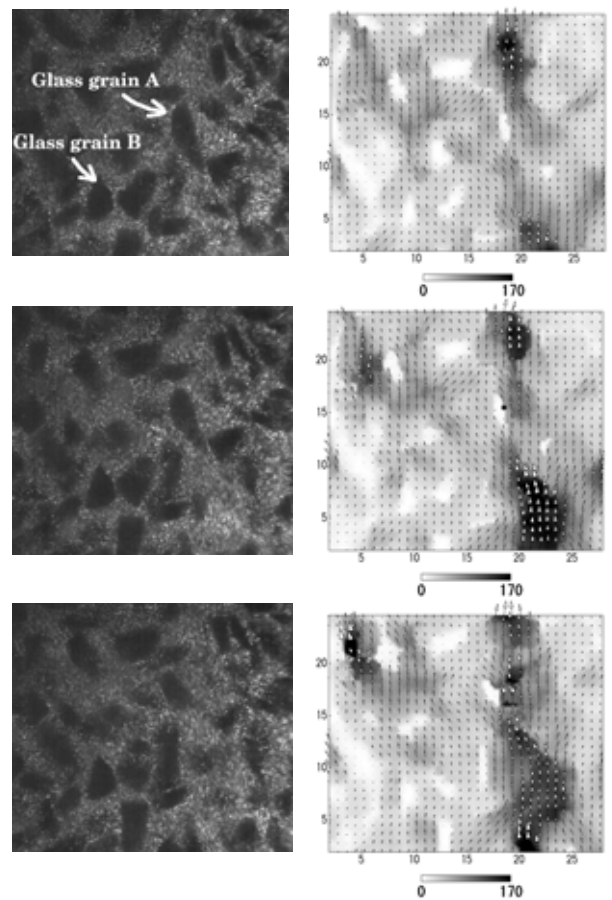Fig.5.4.9. Histograms of vertical velocity component

Fig.5.4.10. Snapshots of boiling
(from top to bottom, t=0.198, 0.252, 0.306 s)

maximum vertical velocity component was as low as 35, which suggests that the intense upward flow during boiling still remains in a laminar flow state. The LAT-PIV can also quantify the configurations of glass grains by tracing the boundaries between the fluorescent powder regions and the no pattern regions.

Figure 11 illustrates the trajectories of two glass grains A and B which are indicated in Fig. 5.4.10. There is an obvious difference in the behaviors of these two grains. The grain A was acutely under the influence of the strong upward flow, causing a heavy anticlockwise rotation reaching to almost 70 degrees and a

Fig.5.4.11. Trajectories of glass grains.

considerable translation within 0.4 seconds. On the other hand, the glass grain B, being positioned out of the strong upward flow, exhibited much less rotation and translation compared with grain A in spite of the small distance between them.

As abovementioned the LAT-PIV technique provides us with attractive information on the behavior of the particle-fluid system. It also has an advantage in terms of scalability, because the resolution shall easily be improved with rapid innovation of digital technology such as those employed in CCD cameras.

5.4.5 DEVELOPMENT THE SPH-DEM METHOD FOR PARTICLE-FLUID SYSTEM

An efficient method, which couples the DEM (Discrete Element Method) with the SPH (Smoothed Particle Hydrodynamics), was developed to directly simulate the particle-fluid system consisting of solid particles and pore fluid. The method called **SPH-DEM** treats both phase as assemblies of particles, which enables us to easily handle a complicated phenomena such as boiling. Because the DEM is well-known and widely used in the field of geotechnical engineering, the details of the DEM is not detailed here.

The SPH, a kind of meshless Lagrangian method, treats the fluid as an assembly of particles. In this method, the standard equation for estimating a physical quantity A at position r is represented by weighted superposition of physical quantity defined by neighboring particles as follows:

$$A(r) = \int A(r')W(r-r',h)dr' \cong \sum_b m_b \frac{A_b}{\rho_b}W(r-r_b,h)$$

where the value of A for a neighboring particle b at position r is denoted by A_b. Notations m_b and ρ_b indicate mass and density of particle b at position r_b, respectively as shown Fig. 5.4.12. W is an arbitrary weighting function called "kernel function" which has a smooth and continuous first derivative and is smooth and continuous itself. Usually the second derivative is also smooth and continuous. Parameters of the kernel function are the distance between position r and position r_b and the scaling variable h. The kernel function also has a restriction for normalization, then weighting function W should satisfy the following equation:

$$\int W(r-r',h)dr' = 1$$

The smoothing formalism also provides a mean to determine gradient of a physical quantity A. The gradient of a physical quantity A at position r is described by

$$\nabla A(r) = \int A(r')\nabla W(r-r',h)dr'$$

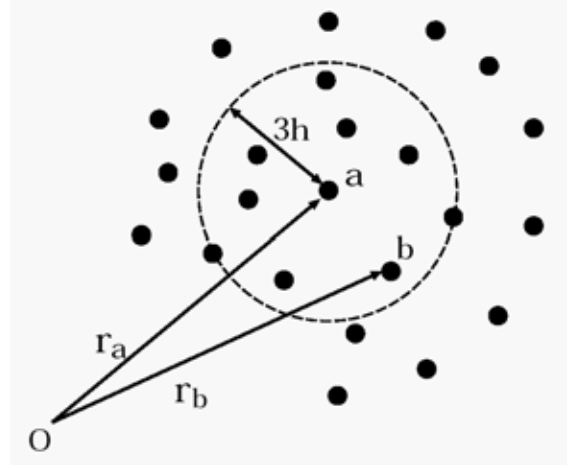$$\cong \sum_b m_b \frac{A_b}{\rho_b}\nabla W(r-r_b,h)$$

Fig.5.4.12. Schematic diagram for SPH formalism.

In this way, the SPH representation of the hydrodynamic governing equations, i.e. Navier-Stokes equations, is empowered. The kernel function W is often represented by the Gaussian function or the spherically symmetric spline function; a function of the later kind, called the quintic spline and expressed as follows, is employed in this study.

$$W(r,h) = \alpha_d \times \begin{cases} (3-s)^5 - 6(2-s)^5 + 15(1-s)^5 : 0 \le s \le 1 \\ (3-s)^5 - 6(2-s)^5 : 1 \le s \le 2 \\ (3-s)^5 : 2 \le s \le 3 \\ 0 : s \ge 3 \end{cases}$$

The notation α_d is a normalization constant which takes $120/h$, $7/(478\pi h^2)$ and $3/(359\pi h^3)$ for one, two and three dimensions, respectively. Symbol S means a parameter $|r_{ab}|/h$, where r_{ab} is a relative position vector between particle a and particle b and $r_{ab} = r_a - r_b$.

In the SPH, the conservation law of mass is satisfied implicitly. The SPH requires ternary processes, i.e. the calculation of the density for each particle, the calculation of the state equation, and the evolution for the equation of motion.

The density is given by,

$$\rho_a = \sum_b m_b W_{ab}$$

where indexes a and b represent the focused particle a nearby particle, respectively; W_{ab} is the kernel value between particle a and particle b.

The equation of motion is expressed as :

$$\frac{dv_a}{dt} = g - \sum_b m_b\left(\frac{P_a}{\rho_a^2} + \frac{P_b}{\rho_b^2}\right)\nabla_a W_{ab}$$

$$+ \sum_b \frac{m_b(\mu_a + \mu_b)v_{ab}}{\rho_a\rho_b}\left(\frac{1}{r_{ab}}\frac{\partial W_{ab}}{\partial r_{ab}}\right)$$

where $\mu = \rho v$ is the dynamic viscosity; P denotes the pressure defined on the particle position and $v_{ab} = v_a - v_b$ is the relative velocity vector between particle a and b. The state equation connecting the density and the pressure is given by

$$P_a = \frac{\rho_0 c^2}{\gamma}\left\{\left(\frac{\rho_a}{\rho_0}\right)^{\gamma} - 1\right\}$$

where ρ_0 is the reference density, c denotes a constant, i.e. fictitious sound speed, and γ denotes another constant related to the compressibility of the fluid. Parameters c and γ govern whether the fluid behaves like incompressible or not.

Since the SPH and the DEM can individually simulate the behaviors of the pore fluid and solid particles in themselves, how to incorporate the interaction between both of them is a key point in the SPH-DEM method.

● : fixed fluid particle
with artificial velocity
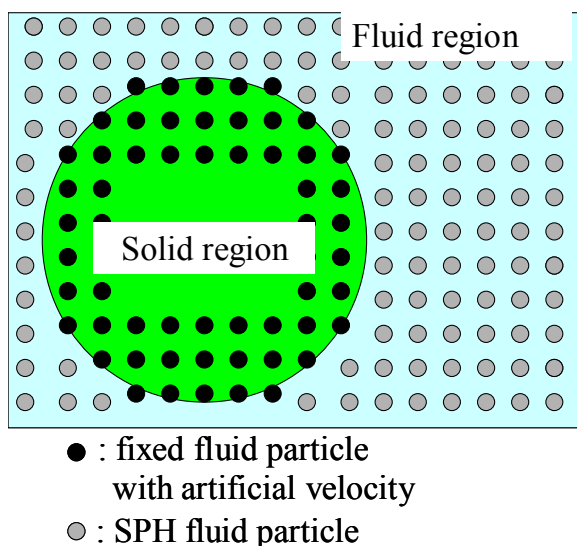
○ : SPH fluid particle

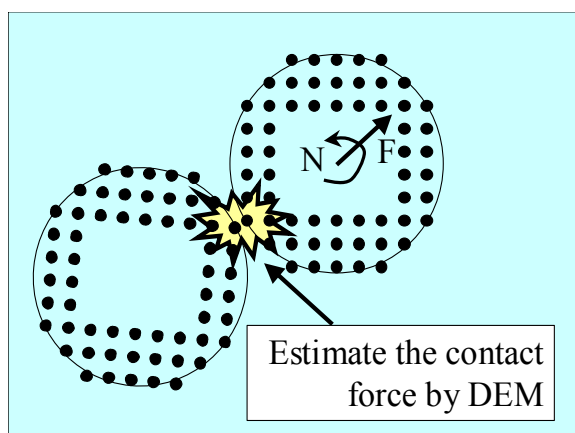Fig.5.4.13. Solid and fluid region.

Fig.5.4.14. Collision of solid particles.

An effective treatment for the boundary between solid wall and SPH fluid particles was introduced by incorporating the artificial velocity into the ghost fluid

particles locating out of the wall in order to satisfy the no-slip condition on the wall surface[14]. We expanded this boundary treatment to the solid particle-fluid particle interaction. The solid particle in the SPH-DEM is modeled by a sets of fluid particle fixed on the solid surface scattering with the reference density of the fluid ρ_0. This arrangement prevents illegal particle penetrations caused by the imbalance of forces arising from the difference in density distribution between the solid region and the fluid region (Fig.5.4.13). The solid particle perceives forces and torques from the fluid on its gravity center by integrating the forces acting on each fluid particle in the solid particle region. The non-slip condition on the solid surface, with a velocity consisting of translation and rotation at the gravity center, is satisfied by controlling the artificial velocities of the fluid particles inside the solid particle. The contact force and torque between solid particles are evaluated by means of the DEM algorithm (Fig.5.4.14), then the acting force and toque are also superimposed at their gravity center. The equations of motion for the solid particles and the fluid particles are separately solved by a time integration scheme after the evaluation of forces.

5.4.6 BOILING SIMULATION BY THE SPH-DEM

To simulate the behaviors of both the solid particles and the pore fluid during boiling, a trial simulation was conducted with the SPH-DEM. Figure 5.4.15 shows the initial state of the simulation model consisting of solid particles (deep-colored regions) and pore fluid particles (light-colored region). Forty solid particles settled in the fluid under gravitational force; each particle of 6 mm diameter was modeled with 29 fluid particles. The periodic boundary condition was used for
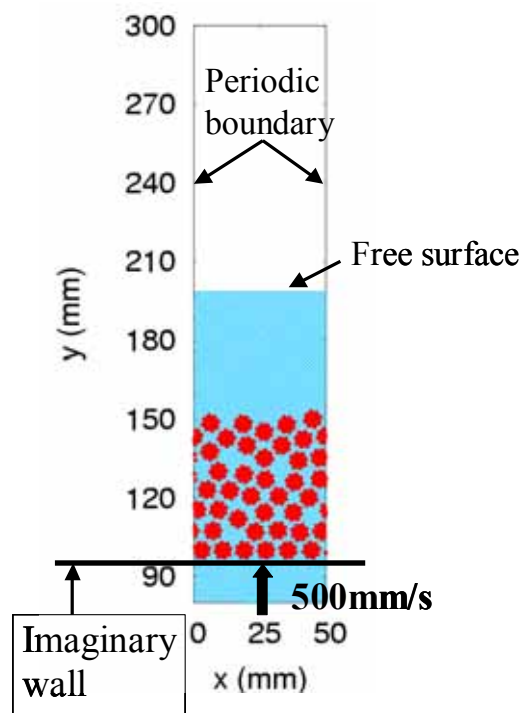

Fig.5.4.15. Initial state of simulation model

the x-direction, meanwhile the top and bottom were treated as free surfaces.

The upward inflow comes from the region ($y \geq 80$mm and 20mm $\leq x \leq 29$mm) with a constant vertical speed of 500 mm/s. The simulation parameters for solid particles and fluid particles are listed in Table 5.4.2 and Table 3, respectively.

Table 5.4.2.   Parameters of solid particle.

Density (g/cm³)	2.52
Diameter (mm)	6
Spring coefficient: normal, tangential direction (g/s²)	1.0×10^5, 0.37×10^5
Damping constant	0.03
Frictional angle (degrees)	26
Critical length for collision (mm)	3.5

Table 5.4.3.   Parameters of fluid particle.

Density (g/cm³)	1.02
Dynamic viscosity (m²/s)	20×10^{-6}
Effective radius (mm)	2.9
Fictitious sound speed (mm/s)	12000
Compression index γ	7

Since it is difficult to model   the three-dimensional real pore structure in   two-dimensional simulation, the "critical length for collision" in Table 5.4.2 was introduced as a parameter to represent the continuity of pore structure. This parameter defines the minimum distance between a pair of solid particles to ensure the pore continuity. The "effective radius" in Tables 5.4.3 is equivalent to the length *3h* shown in Fig. 5.4.12, and its value was determined to be 2.9 mm through a validation of SPH simulating the plane Poiseuille flow. The calculation of 4×10^5 steps with a time increment 1×10^{-5} s corresponds to 4 seconds in real time.

The SPH-DEM can not completely ensure the incompressibility of the pore fluid, which is the case in the experiment, because the method is essentially built on a compressible fluid analysis involving the state equation. Therefore a pseudo incompressible state is employed in such a manner that a small change in the density produces a big pressure change, which is formulated by controlling the parameters γ and c in the state equation.

In the simulation the density change was monitored and limited within a few percents of the reference density; the limit was determined on the basis of the calculation cost or time.

Figure 5.4.16 indicates the density change during the simulation in terms of the maximum and the minimum
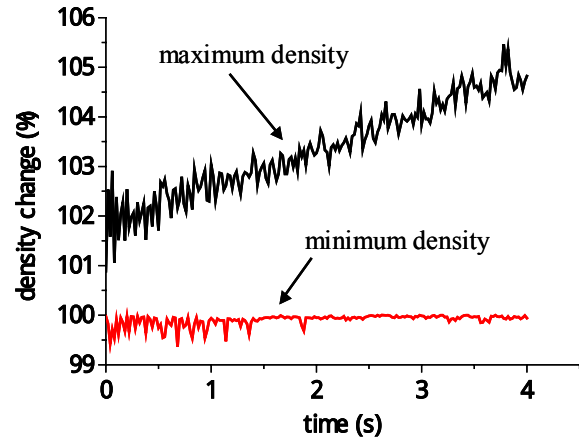

Fig.5.4.16.   Time histories of density change.

densities normalized by the reference density. As shown in this figure the change in the minimum density is consistently less than 1% of the reference density. Meanwhile the change in the maximum density linearly increases with perturbations, which reflects an increase in the hydrostatic pressure due to the rise of fluid surface; the maximum was almost 5% recorded near to the end of simulation. These results suggest that the particle-fluid system approximately stays in an incompressible state during the simulation.

The upper row of Fig. 5.4.17 represents a time series of particle configurations and the lower row illustrates the corresponding particle velocity distributions. The values of color indexes mean the norms of the velocity vectors in terms of millimeter per second. The figures deduces the results as follows:

(1) At 0.3 s, the upward inflow hits the bottom of the solid layer which is still sturdy, then it flows up along the pore structure.

(2) The solid particles locating at the bottom start to split off from the matrix layer which is lifted by the intense inflow. The lift is associated with a localized intense upward flow which subsequently goes up to reach the top of the solid layer at 1.0 s, when the particle splitting stops.

(3) At time 1.7s and thereafter, the solid particles completely disperse, lose the initial matrix form and set in motion a random behavior.

(4) Although the various configurations of the solid particles such as clustering and sparse spacing are seen in Fig.17, localized intense flows always circumvent the clusters of the solid particles.

The SPH-DEM can easily treat the complicated particle-fluid interaction recognized in the boiling. The method is also expected to be useful for studying other phenomena such as liquefaction and piping from a micro-mechanical viewpoint. In order to polish up and validate the applicability of the SPH-DEM, a comparable high-quality experimental data set is necessary. Thus, the SPH-DEM and the LAT-PIV improve complementarily, which leads to the better comprehension of the particle-fluid system.
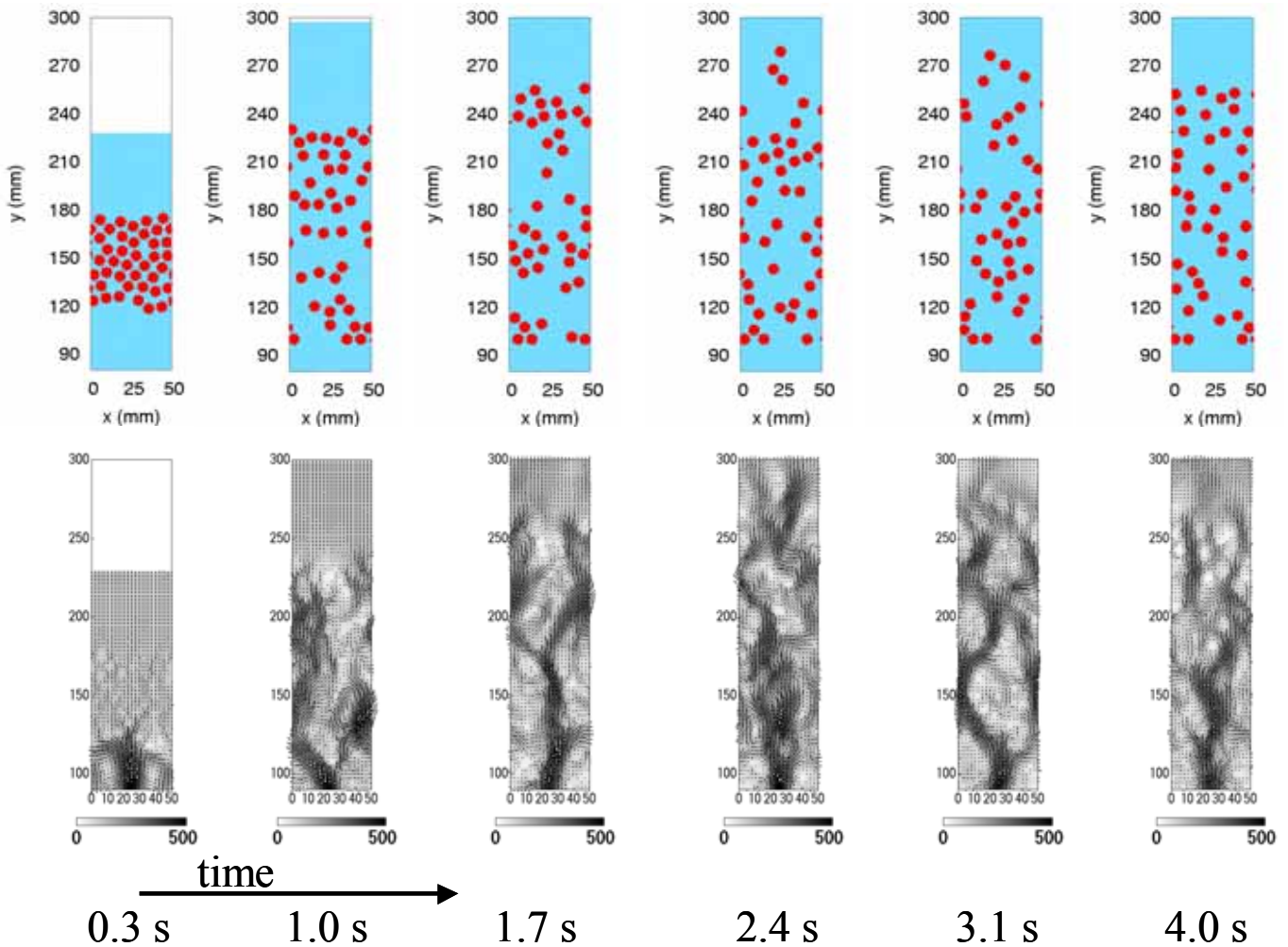
Fig.5.4.17.　Time histories of particle configurations (upper row) and distributions of particle velocities.

5.4.7 CONCLUSIONS

A visualization technique for the particle-fluid system, the LAT-PIV, was developed and applied to permeability tests including seepage failure. The test results are as follows:

The critical hydraulic gradient given by a classical theory and that observed in the experimental was almost the same.

The measured data proved that the Ergun's equation is able to represent the relationship between the mean fluid velocity and the hydraulic gradient with a good accuracy during the seepage state. However it was not applicable to the state of flow whose hydraulic gradient exceeds the critical value.

The distribution of the fluid velocity during seepage state was quantified by the LAT-PIV, and consequently it is clearly recognized as a non-Gaussian distribution.

The distribution of the fluid velocity during boiling was also quantified, then the Reynolds number was calculated on the basis of the maximum vertical component. The Reynolds number was found to be almost 35, which indicated a laminar flow state.

An simulation method for the particle-fluid system, the SPH-DEM was developed and used for the simulation of boiling. As a result, complicated behaviors including particle-fluid interactions were qualitatively interpreted in terms of the clustering of solid particles and the selectivity of fluid pass.

Since the LAT-PIV is essentially a two-dimensional visualization technique, its development for the three-dimensional problems remains as a future prospect. The SPH-DEM is also susceptible to an extension for three-dimensional problems.

REFERENCES

[1] Kobayashi,S., Takahashi,G., Sekiguchi,H.:
Visualization of the Dynamic Interactions of Granular
Media-Pore Fluid Systems by X-ray TV Imaging,
Journal of Applied Mechanics,JSCE, Vol.3, pp.521-531,
2000.(in Japanese)

[2]Konagai,K., Tamura,C., Rangelow, P.and Matsushima,T.:
Laser-Aided Tomography: A Tool for Visualization of
Changes in the Fabric of Granular Assemblage, Structural
Engineering Earthquake Engineering, Vol.9, No.3,
pp.193-201,JSCE,1992.

[3]Matsushima,T.,Ishii,T. and Konagai,K.:
Observation of Grain Dislocation inside PSC Test Specimen
by Laser-Aided Tomography,Soils and Foundations, Vol 42,
NO.5, pp.27-36, 2002.

[4]Matsushima,T., Saomoto,H., Tsubokawa,Y., Yamada,Y.:
Observation of Grain Rotation inside Granular Assembly
during ShearDeformation, Soils¥& Foundations, Vol.43,
Vol.43, No.4,pp.95-106,2003.

[5]M.Raffel, C.E.Willert, J.Kompenhans:
Particle Image Velocimetry (Translation from the English
language edition), Springer-Verlag Berlin Heidelberg,1998.

[6] A.A.Johnson and T.E.Tezduyar:
3D Simulation of Fluid-Particle Interactions with the
Number of Particles Reaching 100,Computer Methods in
Applied Mechanics and Engineering,145,pp.301-321,1997.

[7]David.F.Boutt, Benjamin.K.Cook, Brian J.O.L.
Mcpherson, John R. Williams: Application of a directly
coupled numerical model of fluid-solid mechanics, Third
International Conference on Discrete Element Methods.
[8] L.B. Lucy: A numerical approach to the testing of the
fission hypothesis , Astronomical Journal , Vol.82 ,
pp.1013-1024 , 1977.

[9]R.A. Gingold and J.J. Monaghan: Smoothed particle
hydrodynamics:theory and application to non-spherical stars ,
Monthly Notices of the Royal Astronomical Society , 181 ,
375-389 , 1977.

[10]M.L. Sawley, P.W. Cleary and J.Ha:
Modelling of Flow in Porous Media and Resin Transfer
Moulding using Smoothed Particle Hydrodynamics,
Second International Conference on CFD in the Minerals
and Process Industries, CSIRO, Melbourne, 473-478, 1999.

[11] SABRI ERGUN : FLUID FLOW THROUGH
PACKED COLUMNS ,Fluid Flow Through Paked columns ,
Chemical Engineering Progress , Vol.48 , No.2 , pp.89-94 ,
1952 .

[12]McCabe,Smith and Harriott: Unit Operations of
Chemical Engineering,Mcgraw-Hill,2000.

[13]R.H. Perry,D.W. Green,J.O. Maloney:Perry's Chemical
Engineers' Handbook,Mcgraw-Hill,1997.

[14]Morris, J.P., Fox P.J. and Zhu Y.:Modeling low Reynolds
number incompressible flows using SPH, Journal of
Computational Physics, 136, pp.214-226, 1997.

[15]Saomoto,H :Experimental observation and direct
simulation of particle-fluid system, Doctoral dissertation of
University of Tsukuba, 2004.

[16]Saomoto,H., Matsushima, T. and Yamada.Y:
Development of LAT - PIV Visualization Technique for
Particle-Fluid System, Journal of Applied Mechanics, JSCE,
Vol.8, 2005 (in Japanese, in press).